Designing and characterizing a hardware and software acquisition system for low field MRI

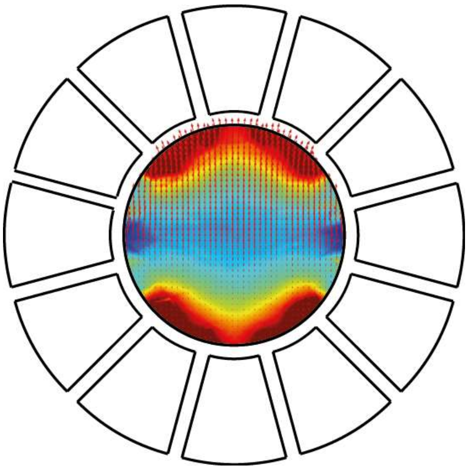

THESIS

Submitted in partial fulfillment of the
requirements for the degree of

MASTER OF SCIENCE
in
PHYSICS

Author:	J. Hockx, BSc
Student ID:	1300598
Supervisor:	Prof. Dr. A.G. Webb
2^{nd} corrector:	Prof. Dr. Ir. T.H. Oosterkamp

Leiden, The Netherlands, June 22, 2017

Designing and characterizing a hardware and software acquisition system for low field MRI

J. Hockx, BSc

Huygens-Kamerlingh Onnes Laboratory, Leiden University
P.O. Box 9500, 2300 RA Leiden, The Netherlands

June 22, 2017

Abstract

A low field MRI software and hardware acquisition system has been designed and characterized. The transmit-receive is not custom built. Instead, a low cost, commercially available Software Defined Radio (SDR) capable of transmission and reception of RF signals was used. An application for the SDR was built using the opensource program GNURadio. The custom built, relevant hardware was a Transmit-Receive switch, a RF probe, and a Halbach array of permanent magnets. The result is a system that can serve as a proof of concept for a low cost, portable, customizable MRI scanner. However, a NMR signal in the form of a Free Induction Decay (FID) remains yet to be detected.

Acknowledgements

I would like to thank Prof. dr. Andrew Webb in several ways. First, for offering a hands-on, research project in the Gorter group. Secondly, for being my supervisor and spending his precious little time left thinking about this projects' problems and opportunities with an open mind. Lastly, for his enthusiasm. But this goes for the whole Gorter Center. It was wonderful to work among so many different people and disciplines. All the help offered is much appreciated. Finally, I would like to thank the Electronics Department (ELD) of the Faculty of Science for their help.

Table of Contents

1. Introduction

The first time Magnetic Resonant Imaging (MRI) was performed on a live human body, was in 1977 [1]. Now, four decades later, the prices for a state of the art MRI scanner can still be as high as three to five million US dollars [2]. A typical clinical MRI scanner uses superconducting electromagnets to create the B_0 field. Super cooling the electromagnets requires a very stable and controlled environment. The magnetic field cannot be switched off, other than in emergency situations and has a large magnetic stray field. Moreover, to reduce the effect of stray fields, the scanner must be placed in a large and protected room that functions as a Faraday cage. In conclusion, the engineering properties of the super cooled hardware are relatively complex. This results in high costs and relatively few companies producing MRI scanners. These companies usually use proprietary hardware parts and software.

Although low field MRI has limitations for the signal strength and the Signal-to-Noise Ratio (SNR) [3], low field MRI can potentially reduce engineering complexities and high costs. With the correct usage of strong permanent magnets, magnetic stray fields can become negligible and even the B_0 field may be turned off [4]. Strong permanent magnets also come at a fraction of the price of a superconducting electromagnet system [5].

Advances in opensource software and consumer radio electronics hardware reduce the costs of transmit and receive systems. Typically, the hardware of such a system is specifically made for a certain application, with a Field Programmable Gate Array (FPGA) at its core. Programming the FPGA involves a steep learning curve and can be tedious for unexperienced FPGA programmers. Instead, Software Defined Radios (SDRs) costing less than a thousand US dollars can be used as the hardware for these systems. Programming is easily done by using the opensource program GNURadio [6].

The goal of this research is to design and characterize a hardware and software acquisition system for low field MRI. This can serve as a prove of concept for a low cost, portable, customizable, crude MRI scanner. Applications for these kinds of scanners can be various, but might especially be relevant to hospitals in developing countries with little funds for MRI scanners. For instance, hydrocephalus is a condition found in 400.000 newborns each year worldwide, leading to suffering and even death. Of these newborns, the majority are born in developing countries (79%) [7]. Cerebrospinal fluid (CSF) accumulation in the brain is the underlying cause of this condition. The accumulated CSF will produce a large enough signal for even crude scanners like the low field MRI scanner and thus the condition can easily be detected at very low costs.

1.1. Outline of this Research

The outline of this research is as follows. First the major physics theories of Magnetic Resonance Imaging are discussed, followed by another theory section on the relevant hardware. The latter details how, in theory, permanent magnets can be used in combination with a Radio Frequency probe, Transmit-Receive switch and an SDR. The Results & Discussion section discusses which permanent magnet array is used. The results of the measurement and simulation of the magnetic field of the magnet array are shown. The design and characteristics for the RF probe are discussed. A major section on all the other relevant hardware used follows, including important results about the Transmit-Receive switch. The section concludes with an overview of all the relevant hardware and the software used for programming the SDR. The section Conclusion and Outlook summarizes the results, concludes and gives suggestions for follow up research.

2. Theory – Physics

2.1. Protons in a magnetic field

The internal spin-angular momentum causes the proton to have a magnetic moment. When an external magnetic field is absent, the moments of the protons are randomly distributed and there is zero net magnetization. When an external magnetic field is applied however, the magnetic moments align parallel or anti-parallel to the magnetic field at an angle of 54.7 degrees. This results in slightly more protons aligned in the parallel direction and causes a net magnetization in the parallel direction [3]. This is visualized in Figure 1.

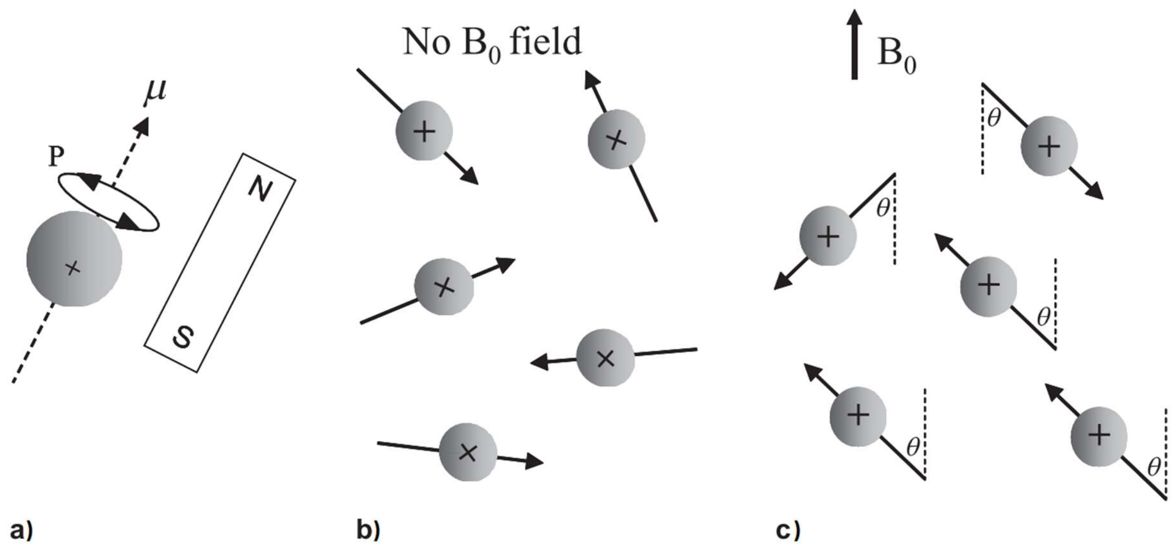

Figure 1 – In figure a, the proton is shown having an angular momentum P, causing a magnetic moment μ. In b) and c), the magnetic moment orientations are shown, with no magnetic field and an external magnetic field B_0 applied respectively [3].

This splitting is known as the Zeeman effect. This quantum effect causes the protons to split into two different energy levels, with an energy difference of:

$$\Delta E = \frac{\gamma h B_0}{2\pi} \tag{1}$$

Where ΔE is the energy difference between the two states, γ the gyromagnetic ratio, h Plank's constant and B_0 the uniform external magnetic field[1].

A magnetic moment in an external magnetic field also processes. The angular frequency can easily be determined by solving classical mechanical equations related to the magnetic moment, external magnetic field and the torque. Solving these equations give rise to the angular frequency, also called the Larmor frequency [3]:

$$\omega_0 = \gamma B_0 \tag{2}$$

2.2. The MR-signal

By using the Boltzmann equation and Equation (1), the difference in the number of protons between states can be calculated. The Magnetic Resonance (MR) signal scales with this difference as:

[1] Throughout this Chapter, we assume B_0 is oriented along the z-direction

$$MR\ Signal \propto N_{parallel} - N_{anti-parallel} = N_{total}\frac{\gamma h B_0}{4\pi k_B T} \tag{3}$$

N is the number of protons (parallel, anti-parallel and total), k_b is the Boltzmann constant and T is the temperature. When all the individual magnetic components are added, the x and y-components average out and only a z-component remains. This magnetic z-component determines the amount of measured signal and is defined as [3]:

$$M_0 = \sum_{n=1}^{\text{Ntotal}} \mu_{z,n} = \frac{\gamma h}{4\pi}\left(N_{parallel} - N_{anti-parallel}\right) = \frac{\gamma^2 h^2 B_0 N_{total}}{16\pi^2 k_b T} \tag{4}$$

When imaging a patient, the total number of protons (N_{total}) as well as the (body) temperature (T) cannot be modified. The field strength (B_0), however, can be modified, with higher magnetic fields giving rise to higher MR signal.

2.3. RF pulse

With M_0 orientated along the z-direction, it is not possible to pick up any signal by magnetic induction. However, tipping M_0 to the x- or y-axis will cause M_0 to rotate in the xy-plane with an angular frequency of ω_0. The tipping of M_0 can be accomplished by applying a transverse magnetic field, B_1, to the x- or y-axis with a frequency of ω_0 (i.e. a RF pulse). This will rotate M_0 to the y- and x-axis respectively. The tip angle is given by:

$$\alpha = \gamma B_1 \tau_{B_1} \tag{5}$$

Where α is the tip angle and τ_{B_1} is the pulse time of the RF signal. The concept is illustrated in Figure 2. Creation of a B_1 field can be achieved by a RF probe (see next Section).

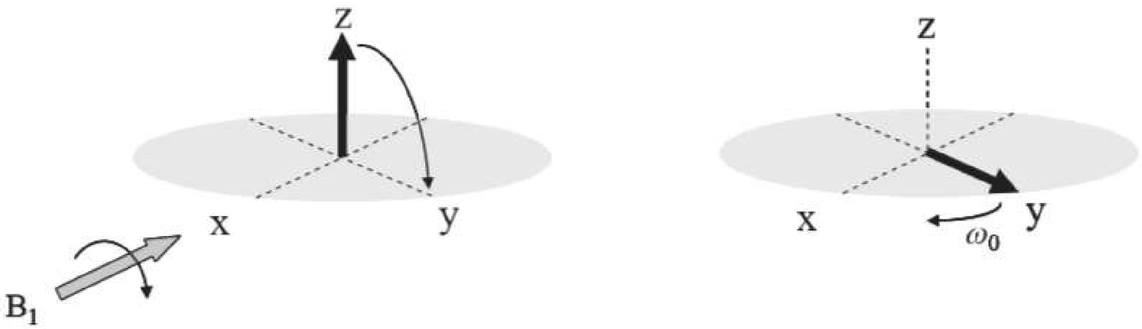

Figure 2 – Application of a B_1 magnetic field along the x-axis (with the correct frequency), tips M_0 with an angle of 90° to the y-axis. After tipping, M_0 rotates in the xy-plane with the Larmor frequency. This assumes a τ_{B_1} such that $\alpha = 90°$.

After the pulse and rotation, the system returns to equilibrium. Two relaxation times are involved: T_1 affecting z-magnetization and T_2 affecting x- and y-magnetization. Solving the Bloch equations that describe relaxation, gives rise to the following relations[2]:

$$M_z(t) = M_0 \cos\alpha + (M_0 - M_0\cos\alpha)(1 - e^{-\frac{t}{T_1}}) \tag{6}$$

and

[2] Assuming a B_1 field applied along the x-axis and a rotating reference frame at the Larmor frequency

$$M_y(t) = M_0 \sin\alpha \, e^{-\frac{t}{T_2}} \tag{7}$$

In practice, there is a small spread in frequencies between the protons. This is the mechanism behind Equation (7) and can be visualized as spreading out of the vectors spreading out over time. T_1 and T_2 relaxation times differ between tissues and can thus be used, for example, in determining which tissue is healthy and which diseased [3].

2.4. Magnetic Resonance Imaging

After applying a RF pulse to the RF probe, the spins are tipped and a signal can be acquired by a coil per Faraday's law (Equation (14), see Section 3.3). As for transmission of a RF pulse, a signal can be detected by using a LC resonant circuit tuned to the Larmor frequency. In fact, since the frequency is the same for transmission and reception, the same coil might be used. Taking the relaxation times into consideration, the induced signal will decay over time. This phenomenon is called the Free Induction Decay (FID).

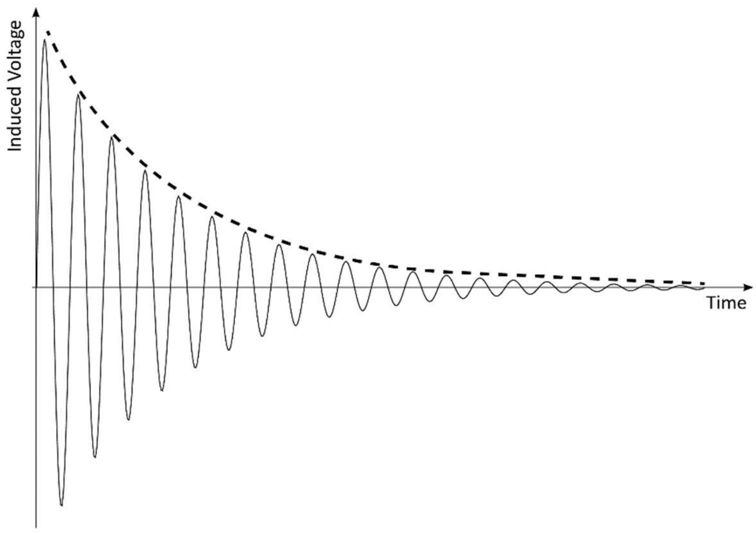

Figure 3 – Free Induction Decay (FID). The solid line is without a rotating reference frame, oscillating with the Larmor frequency. The dashed line is with use of a rotating reference frame at the Larmor frequency. Derived from [8].

To perform Magnetic Resonance Imaging (MRI), spatial information must be encoded into the system. This can be achieved by applying a gradient of an extra magnetic field to the system. The easiest and most commonly used gradient is a linear gradient. If a linear gradient would be applied along the z-axis, the following relation holds:

$$B_z = B_0 + zG_z \tag{8}$$

With G_z the gradient along z. The precession frequency then becomes a function of the position along the z-axis:

$$\omega_z = \gamma B_z = \gamma(B_0 + zG_z) \tag{9}$$

And spatial information is added to the system. Using the k-space formalism, an image can be acquired and reconstructed. The theory on this subject exceeds the scope of this thesis, but is thoroughly explained in [3].

3. Theory – Hardware

3.1. Magnetic field

As seen in Equation (2), any inhomogeneity in the magnetic field will give (slightly) different Larmor frequencies. Consequently, much like T_2 relaxation, the vectors in the rotating reference frame will spread out over time. Because of the similarities with the T_2 relaxation, the effect due to a not completely perfect homogeneous field is characterized by the ${T_2}^+$ time. The combination gives the total T_2 relaxation time, defined by [3]:

$$\frac{1}{T_2^*} = \frac{1}{T_2^+} + \frac{1}{T_2} \tag{10}$$

Magnetic fields in conventional MRI are created by using superconducting electromagnets. For this research, however, permanent magnets placed in a Halbach array are used. A Halbach magnet array is defined as a specific configuration of permanent magnets, that causes the increase of magnetic flux on one side/inside and reduces the magnetic flux on the other side/outside [4]. This is visualized in Figure 4, where illustrations of a possible linear, circular and spherical configuration of Halbach magnets are shown.

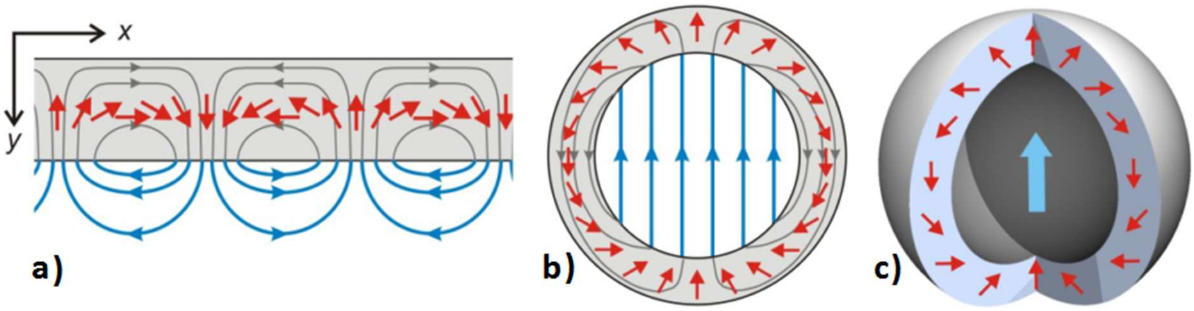

Figure 4 – a), b) and c) are an illustration of a linear, cylindrical and spherical Halbach magnet array respectively. The red arrows indicate the magnetic field vectors at different locations, the blue and gray lines depict the magnetic flux externally and internally respectively [4].

The use of permanent magnets in a Halbach array decrease the stray fields immensely compared to conventional MRI and removes the challenging engineering of a superconducting electromagnet. However, the configurations illustrated in Figure 4 are ideal situations. All configurations assume a continuously changing magnetic field and in a.) and b.) it is assumed that the plate and tube are infinitely long. In reality, it is nearly impossible to make a continuously changing magnetization angle without discretization of the magnet. Some solutions proposed to this problem, are to make good approximations to the ideal Halbach array configuration and are shown in Figure 5.

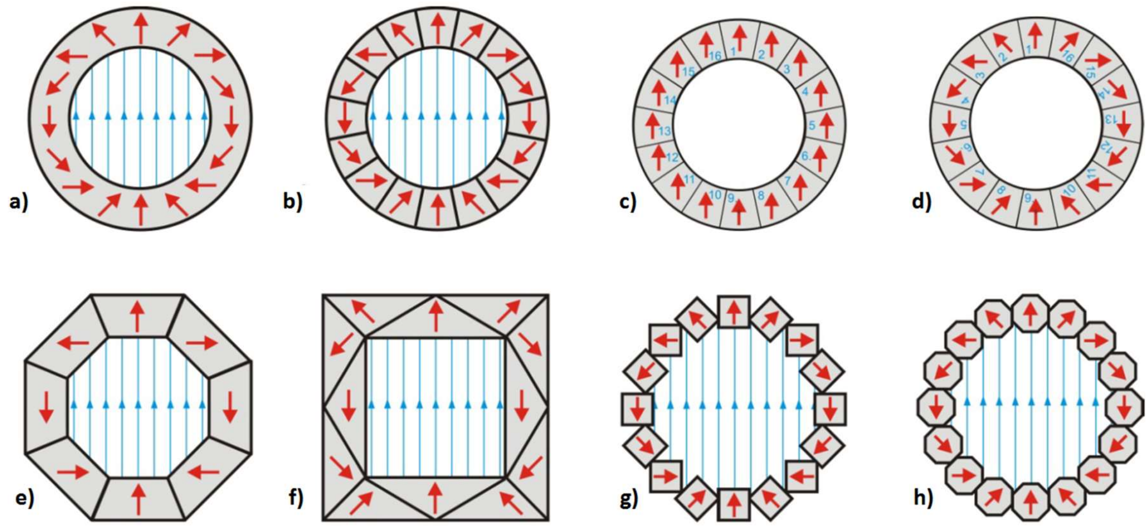

Figure 5 – Possible approximations to an ideal Halbach magnet, using discrete magnet elements. a) Ideal magnet, with continuously changing angle. b) Approximation to a) by discretizing into an array of magnet elements. c) Shows how in practice a circular piece of ferromagnetic material can be magnetized, cut and d) rearranged in a Halbach array. e) f) g) h) Other configurations that approximate the ideal Halbach array in a). [4]

The ideal magnet in Figure 5a can be approximated by having discretized permanent magnet elements made of ferromagnetic material. This is shown in Figure 5b. Figure 5e-h show other configurations that are a good approximation to the ideal case [4].

3.2. T/R switch

To tip the spins of the sample in a magnetic field, a high-power RF pulse is needed. Thus, for brief periods of time high power is applied to the hardware system. These bursts of high power are potentially damaging for hardware at the receiving end (e.g. the preamplifier and receiver). One could potentially use two separate probes or series of probes: one for transmitting and one for receiving[3]. If correctly positioned, it is possible to have little energy transfer from the transmitting probe to the receiving probe. However, this specific placement is not practically convenient, since a slight change in the position of the system can still damage the receiving end of the hardware. This might be solved by incorporating an electrically engineered system that temporarily disables the access of receiving signals to the receiving end during transmission [9]. However, the use of a two-probe-system is not always practical, for example due to dimensional limitations.

The use of a probe that is designed for transmission as well as reception needs protection on the receiving end of the hardware. In the rest of this section, a Transmit-Receive (T/R) switch is discussed as a protection for the receiving end of the hardware.

The simplest electrical scheme functioning as a passive T/R switch shown in Figure 6, was first proposed by Lowe and Tarr in 1968. Here passive is referred to the ability of the T/R switch to operate without an external (TTL) signal. Usage of a physical switch or relay is not possible, as they generally switch too slowly ($> 5\ ms$) and tend to have a certain amount of bouncing [10].

[3] Referred to as a “two-probe-system” (including the serialized version of the system)

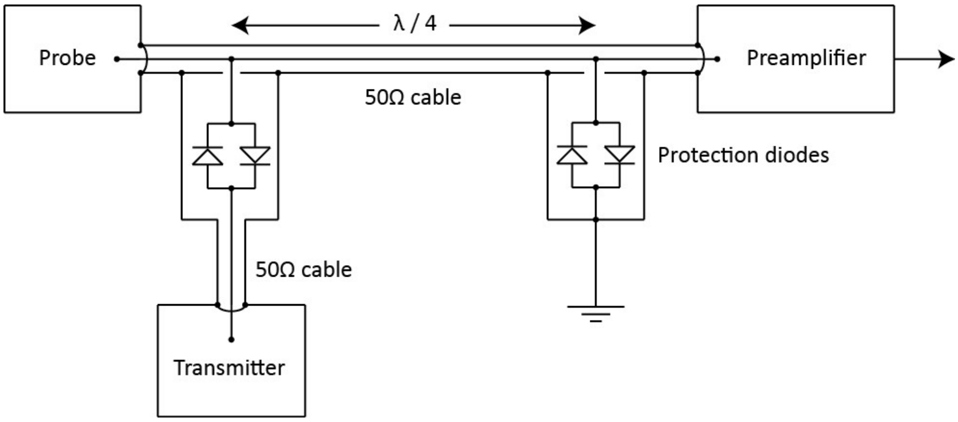

Figure 6 – A passive T/R switch capable of protecting the receiving end of the hardware (here consisting of a preamplifier). On the left side is the transmitter with two crossed diodes before the probe (farther left) and a λ/4 cable (where λ corresponds to the wavelength of the resonance frequency in question). On the right side are protection diodes (connected to ground) and a preamplifier. A RF signal (at the resonance frequency) travels to the preamplifier, only if the signal is below the forward voltage (V_{fw}) of the crossed diodes. If the signal is higher than V_{fw}, the signal strength is attenuated to ~ V_{fw} [10].

The first set of diodes block any noise from the transmitter (e.g. power amplifier) to the probe and receiving end during reception. In addition, any signal generated in the probe will not travel into the transmitter during reception. In this scheme, the $\lambda/4$ cable is crucial. The relation between impedances for this cable is [11]:

$$\frac{Z_{in}}{Z_0} = \frac{Z_0}{Z_{out}} \tag{11}$$

Z_0 is the characteristic impedance, Z_{in} the input impedance and Z_{out} the output impedance. Assuming the hardware system is completely impedance matched at $Z_0 = 50\ \Omega$, the input impedance goes to infinity in the limit of Z_{out} going to zero (or when $Z_{out} \ll Z_0^2$). The protection (crossed) diodes on the right side short circuit if the voltage of the RF pulse is larger than the forward voltage of the diodes. Energy dissipation in the diodes is negligible. When shorted, the output impedance is nearly zero. Consequently, the input impedance is extremely large ($Z_{out} \gg 50\ \Omega$), reflecting most of the incoming RF wave. Thus, most of the power is applied to the probe (left side) with an impedance of just $50\ \Omega$. However, for low frequencies the length of the cable becomes impractically long. Moreover, this introduces losses of the signal and increases the susceptibility of interference, lowering the SNR.

A solution to these problems, is replacing the $\lambda/4$ cable by a lumped element circuit. Specifically, a π-section filter as shown in Figure 7 can be used as replacement.

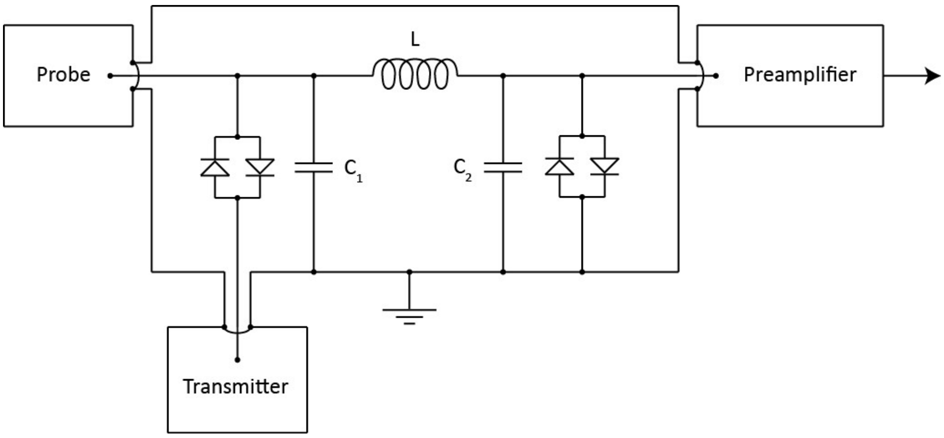

Figure 7 – Replacement of the λ/4 cable in Figure 6 by a lumped element circuit (π-section filter), consisting of two capacitors (C_1, C_2) and an inductor (L) [10].

This filter maintains the $50\ \Omega$ impedance at the resonance frequency, but functions as a LC-filter when the protection diodes conduct (C_2 is bypassed, leaving a LC-filter consisting L and C_1) [10]. Thus, the resonance frequency as a function of the capacitance and inductance can be determined as follows [12]:

$$\frac{1}{Z_0} = \frac{1}{Z_L} + \frac{1}{Z_C}$$

Rewriting gives:

$$Z_0 = \frac{Z_C Z_L}{Z_L + Z_C} = \frac{i\omega L}{1 - \omega^2 LC}$$

In a state of protection, the impedance goes to infinity. In other words, when:

$$\omega^2 LC = 1$$

Thus, resulting in:

$$f_{res} = \frac{1}{2\pi\sqrt{LC}} \quad (12)$$

The lumped element T/R switch is never ideal and a short by the protection diodes may not be perfect. These switches generally don't exceed an attenuation of $-40\ dB$ in power. To improve, it is possible to add several $\lambda/4$ cables or π-section filters with corresponding protection diodes. However, one must be careful with these additions as more noise is added to the system, degrading the SNR [13].

3.3. RF probe

As described in Section 2.3, a B_1 field applied along the x-axis can tip the M_z component of M_0 to the y-axis. The tip angle is described by Equation (5). A B_1 field can be created by passing a current through a copper coil. Classical electromagnetism describes a magnetic field perpendicular to the windings of the coil as follows:

Using Ampère's law, one can derive the magnetic field of an infinitely long solenoid with n closely wound turns per unit length. Assuming a solenoid oriented along the z-axis, one comes to the following relations:

$$\boldsymbol{B} = \begin{cases} \mu_0 n I \hat{z} & \text{inside the solenoid} \\ 0 & \text{outside the solenoid} \end{cases} \tag{13}$$

Where $\boldsymbol{B}$ represents B_1 for an infinitely long coil, μ_0 is the permeability of free space, n the number of windings per unit length and I the current [14]. In practice, it is impossible to have a solenoid of infinite length. Instead, a small solenoid might have a B_1 field described by Equation (13) exactly at the center of the coil ($z = 0$) gradually reducing to one half its maximum value at the ends. The intensity of the signal depends on the x- and y-component of M_0. Moreover, as the x- and y-component of M_0 rotate in the xy-plane, a voltage (i.e. signal) is produced in any coil perpendicular to the x- or y-axis according to Faraday's law of induction [3], [14]:

$$V \propto -\frac{d\phi}{dt} \tag{14}$$

Where V is the induced voltage, ϕ is the magnetic flux and t is the time. From this, it follows that the y- and x-component are related to M_0, the Larmor frequency and time in the following way [3]:

$$\begin{aligned} V_y &\propto M_0 \omega_0 \, sin \, \omega_0 t \\ V_x &\propto -M_0 \omega_0 \, cos \, \omega_0 t \end{aligned} \tag{15}$$

In practice, a resonance circuit is used to produce an oscillating B_1 field at the Larmor frequency. A classical (parallel) LC-circuit can function as this resonance circuit, where the inductor obviously consists of the solenoid. This is illustrated in Figure 8.

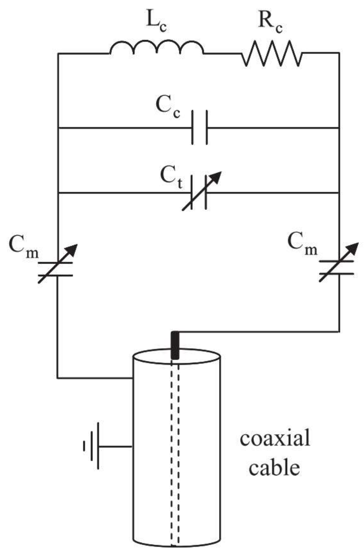

Figure 8 – L_c, C_c and R_c form the basic resonance circuit for the creation of a RF pulse. L_c consists of the solenoid, which produces the B_1 field. R_c is the resistance of the copper wire, although extra resistance can be added to increase the bandwidth. C_t is a tuning capacitor, to fine tune to the correct frequency. Both C_m capacitors match the impedance of the probe to the coaxial cable [3].

Most coaxial cables have an impedance of $50\ \Omega$. Two capacitors are added to balance and impedance match the circuit to the coaxial cable. Impedance matching will result in the least signal losses [3]. The resonance frequency of the circuit is:

$$f_{res} = \frac{1}{2\pi\sqrt{LC}} \tag{16}$$

Where $C = C_c + C_t$ and $L = L_c$. When using a solenoid as the inductor, the following relation exists:

$$L = \frac{\mu N^2 A}{l} \tag{17}$$

Where μ is the permeability of the matter inside the solenoid (most conveniently $\mu = \mu_0 \sim \mu_{air}$), N are the number of windings, A is the surface area and l the length of the solenoid. Thus taking Equation (16) and (17) together, one is able to determine the number of windings for the solenoid based on the radius, the Larmor frequency ($f = f_0$) and the value of the abitrarily (though practically) chosen capacitor (C).

$$N = \sqrt{\frac{l}{C\mu A}\frac{1}{2\pi f}} \tag{18}$$

3.4. Transmit-receive systems

Inhouse built systems

In house constructed transmit-receive systems can be quite complex. For example, W. Tang, H. Sun and W. Wang [15] designed a digital receiver system using a Digital Receiver Module, Digital Exciter Core and a Master Controller. These modules in turn consist of several other components, like a Direct Digital Synthesizer (DDS), Digital Signal Processor (DSP) and a Field Programmable Gate Array (FPGA). These components are used more often in transmit-receive systems. For instance, the transmit-receive system designed by A. Asfour, K. Raoof and J.P. Yonnet [16] is schematically shown in Figure 9. The major modules involve a DDS, DSP and a SDR instead of a FPGA. It must be noted that everything was custom built, including the SDR. The three major modules are designed using a large array of other components not shown here.

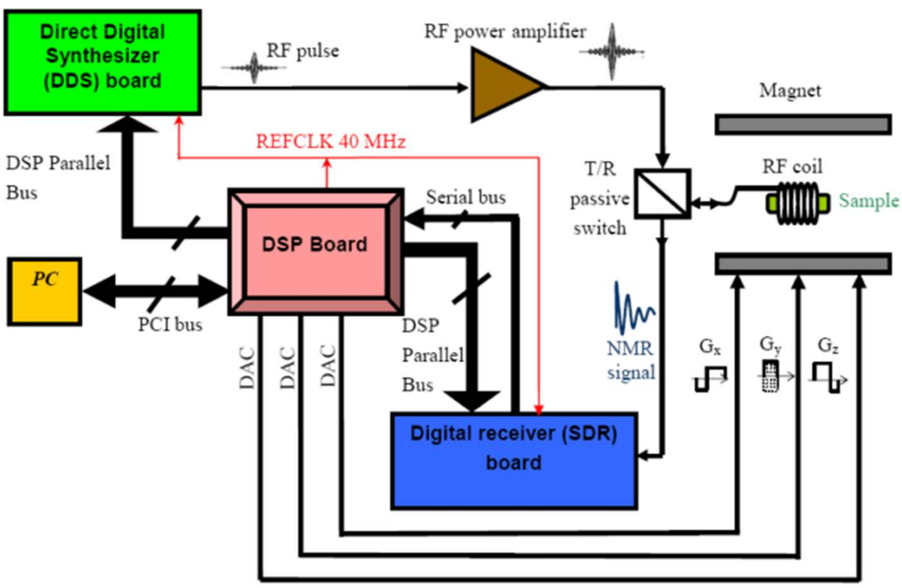

Figure 9 – Transmit-receive system as designed by A. Asfour, K. Raoof and J.P. Yonnet [16]. *The major modules are the Direct Digital Synthesizer (DDS), Digital Signal Processor (DSP) and the Software Defined Radio (SDR). All these modules are custom build and consist of more components not listed here.*

Systems using a Software Defined Radio

Custom built systems like the ones mentioned in the previous section, can be simplified by using a Software Defined Radio as the core of the system [6]. This is schematically illustrated in Figure 10. The SDR can easily be programmed with use of the free, opensource software GNURadio [17]. GNURadio applications can be written in C++ or Python. To simplify the use of GNURadio, the software comes with the GNURadio Companion. This lets the user generated python files visually, with the use of "blocks". For more advanced software engineering, it is possible to create custom blocks in C++ or Python [18].

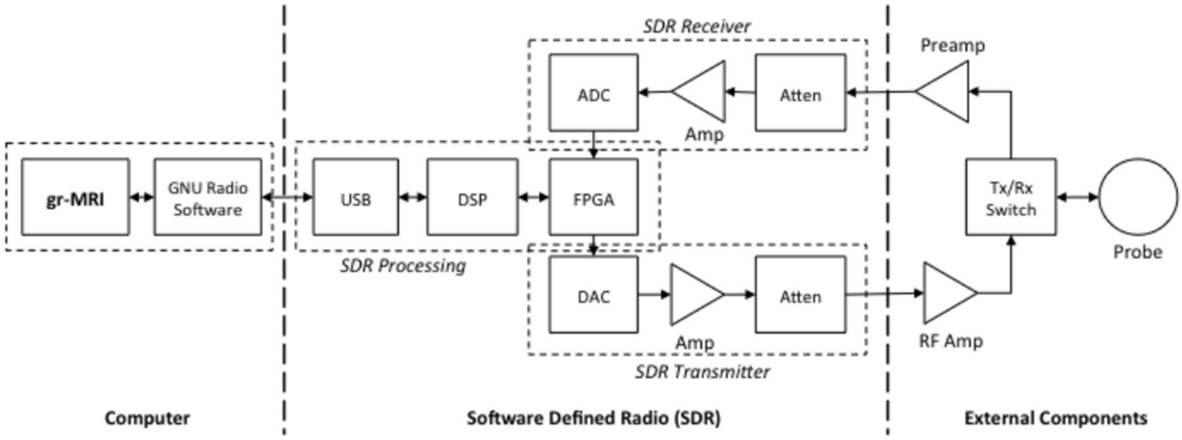

Figure 10 – A simplified transmit-receive system using a Software Defined Radio (SDR). The SDR handles all transmission, reception and processing of signals. Only the external components and computer program must be taken into consideration in the design of the transmit-receive system. In this example, the software is extended with the gr-MRI packages [6].

3.5. Challenges

The net magnetization component M_0 is dependent on B_0 (Equation (4)). The signal Larmor frequency too, depends on B_0 (Equation (2)). From Equation (15) it then follows that the NMR signal (V_y or V_x) scales with B_0^2. Moreover, the SNR scales with $B_0\sqrt{B_0}$ [3]. The ability to pick up a NMR signal and to filter a signal from the noise, all depend on the B_0 magnetic field of the MRI scanner. Therefore, low field MRI is challenging and is used little clinically. As mentioned in the Introduction however, there are several reasons why low field MRI scanners could be useful, like cost reductions and diagnosing diseases that do not require top of the line MRI scanners. The next Chapters will go into detail of the design and characterization of a hardware and software acquisition system for low field MRI.

4. Results & Discussion

4.1. Halbach Magnet Array

For the creation of a B_0 field, permanent magnets were used as elements in a Halbach array with magnets consisting of Neodymium (NdFeB) with 3 layers of coating. The Nickel-Copper-Nickel (Ni-Cu-Ni) coating prevents the Neodymium material from corrosion. All elements are of the same dimensions and have the same magnetic field strength, but differ in magnetic field orientation (Figure 11a-b).

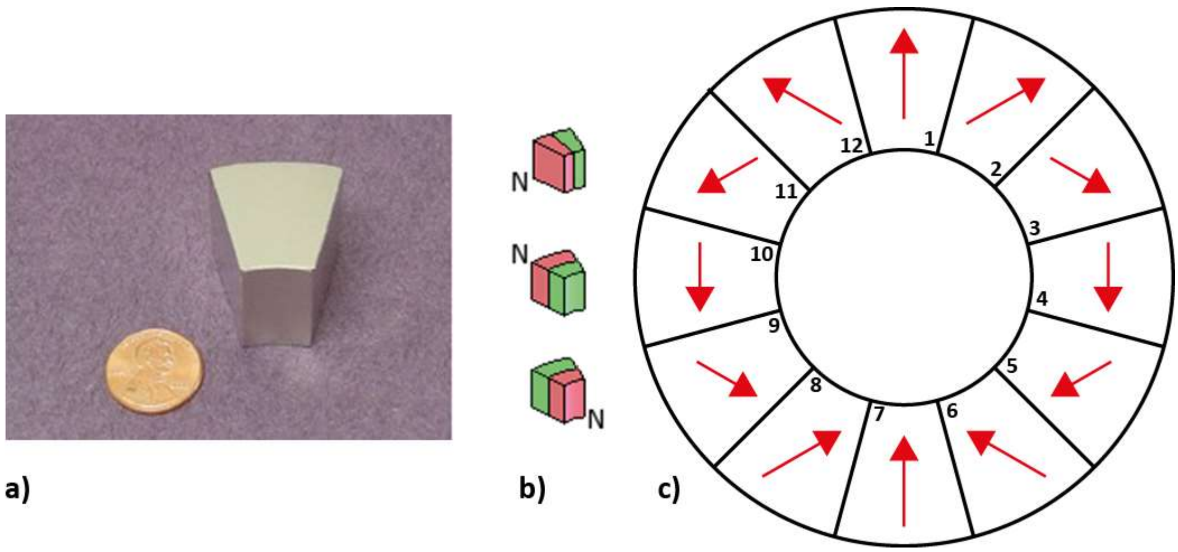

Figure 11 – a) A neodymium magnet element with a coin for size reference. Dimensions: outer radius 50.8 mm (2") x inner radius 25.4 mm (1") x 25.4 mm (1") x 30°. b) Three possible magnetic field orientations of the magnet elements [5], [19]–[21]. *c) The magnet elements configuration used in this research.*

The elements were placed in an array as shown in Figure 11c. This was done by making a former of polymethylmethacrylate (PMMA) with a laser cutter. This caused the elements to have some spacing between each element ($3\ mm \pm 0.05\ mm$).

The finite elements in the array cause the B_0 field to be inhomogeneous. The field has a gradient in all three directions. In the x- and y-direction it is similar to that of a 2-dimensional parabolic structure, while the gradient in the z-direction is less strong.

4.2. Measuring method

The magnetic field was measured using a magnetic field probe. The probe consisted of a small Hall effect sensor inside a plastic tube. Two laser cut measuring plates with a grid of circular holes could be attached to either side of the magnet. The plastic tube is then slid through these holes on both sides, thus remaining parallel relative to the bore of the magnet for each measurement. This is under the assumption that the plates are placed exactly opposite of each other. To hold the magnetic sensor in the exact same place *inside* of the plastic tube for all measurements, a piece of foam was placed inside the tube.

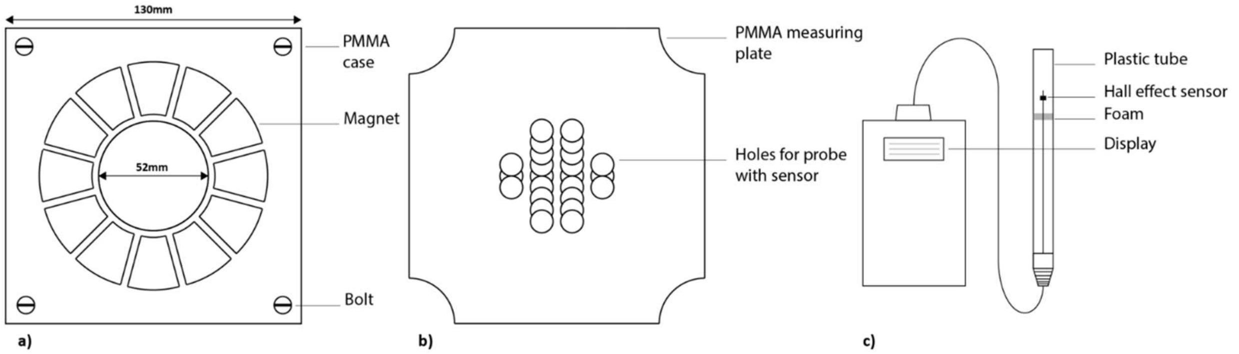

Figure 12 – a) PMMA former for the magnets. b) PMMA measurement plate. Mounted on the front and back during measurement. The plastic tube with the sensor inside, c), is slit through the front and back measurement plate. This locks the x- and y-position of the tube. Five different z-positions were measured.

The spacing from center to center between the (measuring) holes in the y-direction was 5 mm. For practical reasons, this was slightly more in the x-direction: $7.5\ mm$. In the z-direction five different positions were measured. Taking the center of the bore along the z-axis as a reference point (h_0), the other four measuring locations along the z-axis were at $z = \ \pm 4.4\ mm \pm 0.1\ mm$ and $z = \pm 8.8\ mm \pm 0.2\ mm$. The depth of the bore was $40\ mm \pm 0.5\ mm$, including the PMMA former.

4.3. B_0 measurement

In chapter 4.2 the method for measuring the B_0 field was described. For illustration purposes, (only) the results of the field measurements of h_0 are shown below.

y

		405	395	426		
	405	360	344	369	420	
	337	319	308	323	342	
292	297	293	287	295	299	290
277	284	286	279	286	285	278
289	297	294	288	296	300	295
	339	324	310	323	341	
	416	369	344	364	415	
		-	393	-		

a) x

y

		87.4	39.9	-12.6		
	77	45.3	30.9	7	2.3	
	36.6	30.7	31.1	-5.5	27.9	
-1.5	15.7	7.9	25.2	26.6	29.5	44
8.52	27.2	17.6	33.7	31.2	25.4	31.6
30.8	25.8	0	31.4	37.7	37.5	11.1
	28.9	0.2	39.2	57.1	40.2	
	2.9	-11.8	36.3	61.4	84.5	
		-	47.8	-		

b) x

Figure 13 – Magnetic field measurements at h_0 (mT). Positions that were unable to be measured are indicated with a "-" (minus). a) The sensor's plane was placed perpendicular to the y-direction. b) The sensor's plane was placed parallel to the y-direction.

One can easily conclude that the field is not completely homogeneous, as was expected. The lowest values of the magnetic field are exactly at the center, due to trivial symmetry reasons. Near the Neodymium magnets, the values are the highest. All the parallel measurements are not completely zero as in the theoretical, ideal case. Differences in neighboring positions are larger in Figure 13b than in Figure 13a. One explanation is that the physical field has indeed larger deviations, another is that the probe is either bad at measuring lower values or has trouble measuring the field along the x-axis in presence of a much larger field component along the y-axis. Taking both directional components gives a magnetic vector field at h_0:

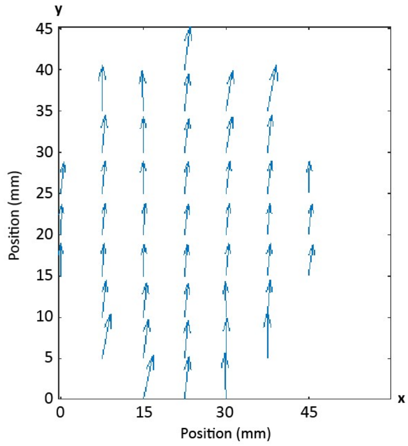

Figure 14 – Vector field of h_0.

It is clear from Figure 14 that the magnetic field is oriented almost entirely along the y-axis, with relatively small deviations in the angle for every position. Figure 13a shows a magnetic field that features parabolic similarities. In fact, by applying a two-dimensional polynomial fit to the magnetic field, it is possible to approximate a continuous magnetic field and thus approximate the inter-positional magnetic field of the individual measurement positions:

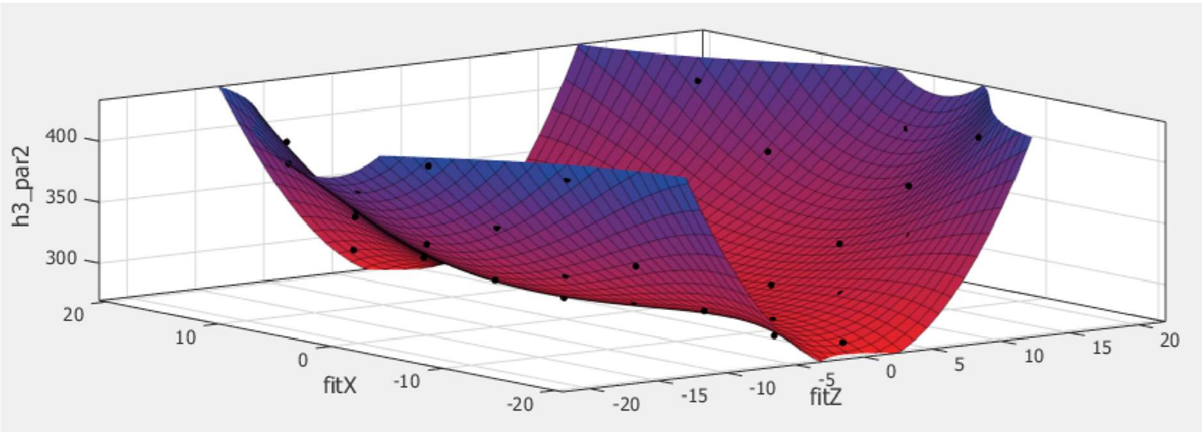

Figure 15 – A two-dimensional polynomial fit of the B_0 field at h_0. [7]

4.4. B_0 measurement remarks

As described in Section 4.2, a Hall effect sensor in a protecting plastic tube was placed inside the bore by making use of measuring plates. While in the z-direction this measuring method was quite accurate, the method lacked freedom of measurement in the x- and y-direction and had a larger than necessary (human) error in the angle. To increase x- and y- measurement freedom, reduce the error in the angle and to have a more accurate parabolic fit, a suggestion for future research is to make use of a machine for all the measurements. With new, cheap and easy to understand technologies emerging, like the Arduino and Raspberry Pi, these kinds of devices become easier to build. Specifically, a few examples can be found among hobbyists. For instance, the do-it-yourself robot arm of Stanley Hou In Lio [22], engineer at University of Southern California and the device of Peter Jansen [23], researcher at the University of Arizona. A second improvement would be to use a newer probe or one that is calibrated more recently, although the differences might be minimal.

The measurement probe used throughout the research was last calibrated in 2006. A new device was bought for better measurements. Although re-measurement for every position was not performed, the center value at h_0 was measured. The magnetic field at this location had a y-component of $291\ mT$. This thus results in a frequency of:

$$\mathrm{f}_0 = \frac{267.513\times10^6\times291\times10^{-3}}{2\pi} = \ 12.4\ MHz \tag{19}$$

Which is exactly the frequency that the RF probe and switch are tuned to. However, $279\ mT$ will give a somewhat lower frequency. Thus, a difference of 12 mT gives a difference in frequency of:

$$\mathrm{f} = \frac{267.513\times10^6\times12\times10^{-3}}{2\pi} = \ 0.5109\ MHz \tag{20}$$

Although the old probe is likely to be less accurate, the difference was still taken into consideration for the bandwidth of the probe. Thus, a bandwidth of $1 - \ 1.2\ MHz$ should suffice.

4.5. B_0 simulation

To get an estimate of the B_0 field and see if the physical B_0 constituted no mayor defects, a simulation of the field was made by M.S. Wijchers [7] in the simulation program COMSOL Multiphysics:

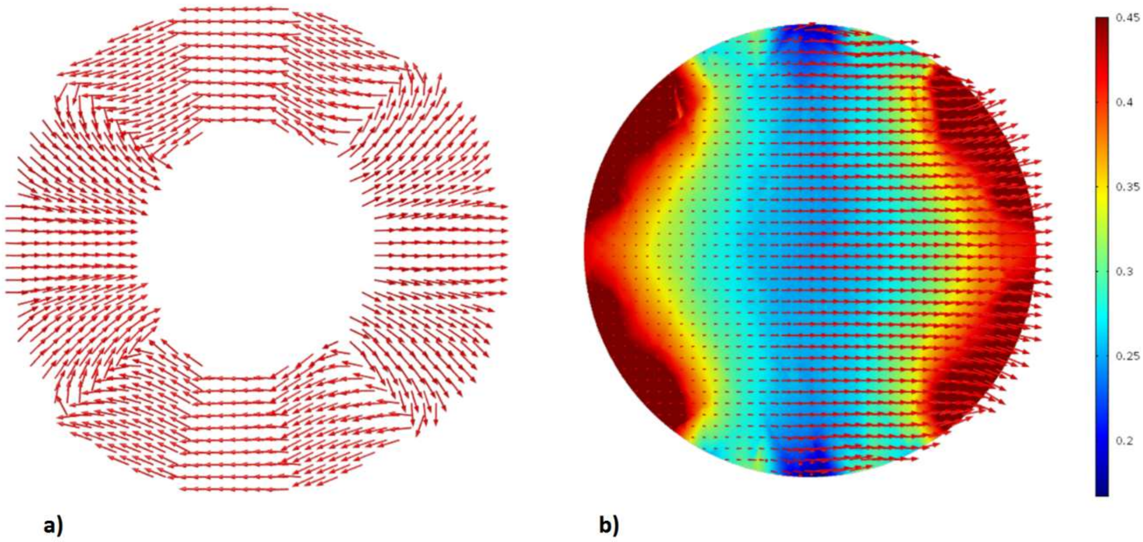

Figure 16 – Simulation of the B_0 field at h_0, modeled in COMSOL Multiphysics. a) Magnetization vectors of the Neodymium magnets in the (x,y)-plane b) Magnetic field strength (T) in the (x,y)-plane. [7]

From Figure 16b it can be concluded that the field at the center is slightly lower ($30\ mT$) and the field at the edges are slightly higher ($60\ mT$) in the simulation than the measured value. M.S. Wijchers suggests this deviation might be assigned to deviations in magnetic strengths in the Neodymium magnets [7]. Another suggestion for these deviations is the fact that the spacing between the neodymium magnets is not zero, but $3\ mm \pm 0.05\ mm$. Although simulations show deviations, the measured physical B_0 field is fairly similar to the simulated B_0 field.

4.6. RF probe

Due to the limited space in the bore of the magnet, transmission *and* reception is accomplished through the same RF probe. The probe follows the design in Figure 8 following the theory described in Section 3.3. A PCB was used in the design and the copper wire was kept to a minimum, to minimize the additional inductance created by the circuit. Following Equation (18), the number of windings was determined after taking $C_c = 137.5\ pF$ and $C_t = 5 - 90\ pF$. The radius and length were an approximation: $l = {\sim}5\ mm$ and $r = {\sim}7\ mm$. The permeability of free space was used for the matter inside of the solenoid (air): $\mu \sim \mu_0 = 4\pi{\times}10^{-7}\ N/A$. With $f = 12.4\ MHz$, this resulted in $N = 6$ windings.

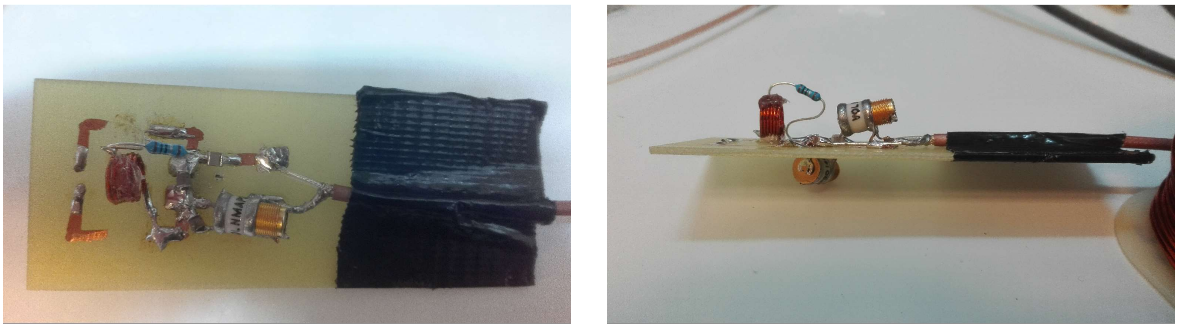

a **b**

Figure 17 – a) Top view of the probe. b) Side view of the probe.

However, the network analyzer revealed that the true resonance frequency was approximately $23\ MHz$. With $f_{res} = 23\ MHz$ and $C = 137.5\ pF$, the true inductance of the LC-circuit was $L = 348\ nH$ (Equation (16)). Again using Equation (16), the capacitance could be calculated back to $C = 473\ pF$. Therefore $C_c = 430\ pF$ and $C_t = 5 - 90\ pF$. The matching capacitors were taken to be $C_m = 100\ pF$ with a extra variable capacitor in parallel to the left matching capacitor. This gave the following Log-Magnitude plot with the network analyzer:

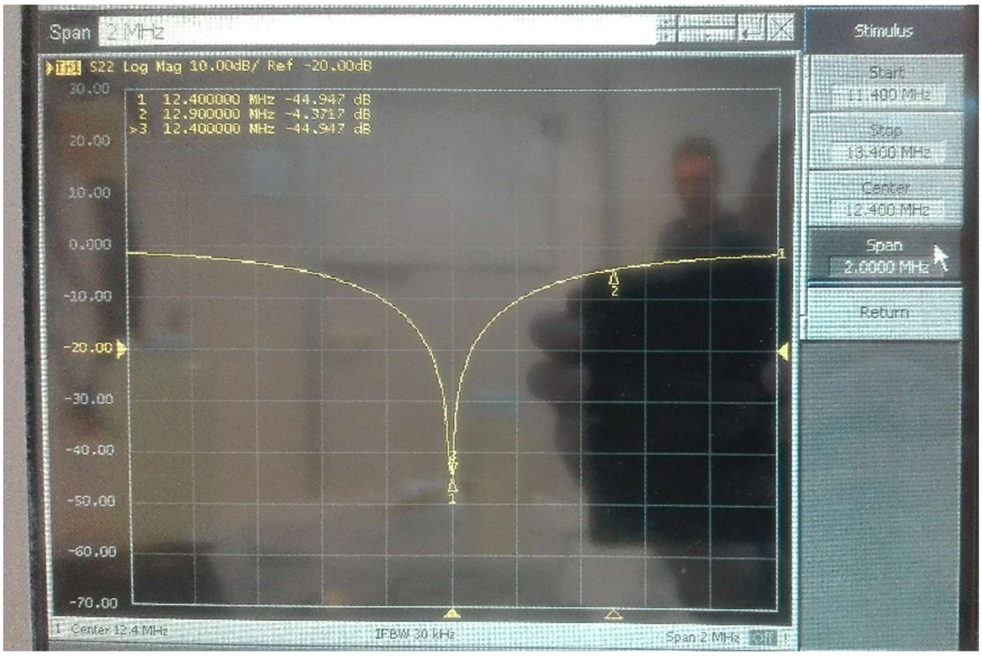

Figure 18 – The resonance frequency of the probe is $f_{res} = 12.4\ MHz$. The S22 measurement shows the reflection to be -44.9 dB. At 12.9 MHz (marker 2) the S22 measurement gives -4.4 dB. Thus, the bandwidth is approximately 1 – 1.2 MHz.

A resistor is added to the LC-circuit to increase the bandwidth to $1 - 1.2\ MHz$. The profile of the Log-Magnitude plot does not change significantly when a phantom is placed inside the solenoid, nor does the minimum change significantly.

For this RF probe a PMMA holder was designed and bolted to the PMMA holder of the magnet. This locks the RF probe in place in the bore during transmission and reception.

4.7. Hardware

To tip the spins of Hydrogen atoms in a sample and sequentially receive a signal from these same atoms, a setup of interconnected hardware is needed. First a signal needs to be generated. In this research, there has been made use of a Software Defined Radio (SDR). This device functions as a true I/O (Input-Output) device, allowing one to simultaneously program sequences of RF pulses and read any incoming signals. Any generated RF pulse first needs to be amplified before entering a RF probe to generate a magnetic flux large enough to tip M_0. This is accomplished by means of a power amplifier. Subsequently, the RF signal will travel into the RF probe through a T/R switch. Since the RF probe cannot transmit *and* receive simultaneously, a T/R switch is incorporated between the transmission-end (Tx), receive-end (Rx) and the probe. Moreover, the switch serves as a delimiter of the transmit- and receive-end. This device can be electrically engineered in such a way that it follows a simple Tx(ON)-Rx(OFF) and Tx(OFF)-Rx(ON) for the transmission- and receive-state respectively (see chapter 3.2). When the switch is in the receive state, any signal generated by the magnetic flux of M_0 will travel through another amplifier, called the preamplifier. This amplifies the very weak signal from the probe, so it fills the analogue to digital converter by the SDR. In addition to these devices, an oscilloscope[4] is used as a measuring device to determine the precision of individual signals in the system.

4.7.1. Software Defined Radio

A system that has inputs and/or outputs for NMR/MRI instruments are generally build by biomedical engineers themselves. Put in other words; every setup of instruments commonly uses 'homemade' components or devices (two examples are [15], [16]). However, these devices tend to be application specific, take a considerable time to be build and are complex in their use. In this research we follow a setup as proposed by C. Hasselwander and W. Grissom [6]. In their research, a commercially available Software Defined Radio from ETTUS research for less than a thousand US dollars is used. This SDR called USRP1 has been used in this research as well. It consists of one motherboard (DC$-6\ GHz$) with up to four daughterboards; two for transmission, two for receiving. There are several daughterboards available with different characteristics. In this research, the LFTX and LFRX daughterboards are used that can output and measure RF signals in the range of $\pm 1\ V$ and in the frequency range between DC and $30\ MHz$.

4.7.2. Power amplifier

The power amplifier used could amplify RF signals up to $20\ W$.This device was rather large, but a small, portable power amplifier in the correct frequency range is not widely available. The noise levels measured when the output of the USRP1 was directly connected to the oscilloscope, were $0.25\ mV$. However, when the power amplifier was placed in between, the noise levels rose to $2\ mV$. Distortion in the RF signal directly after amplification was minimal.

[4] Every measurement on the oscilloscope is done with 50 Ohm input impedance.

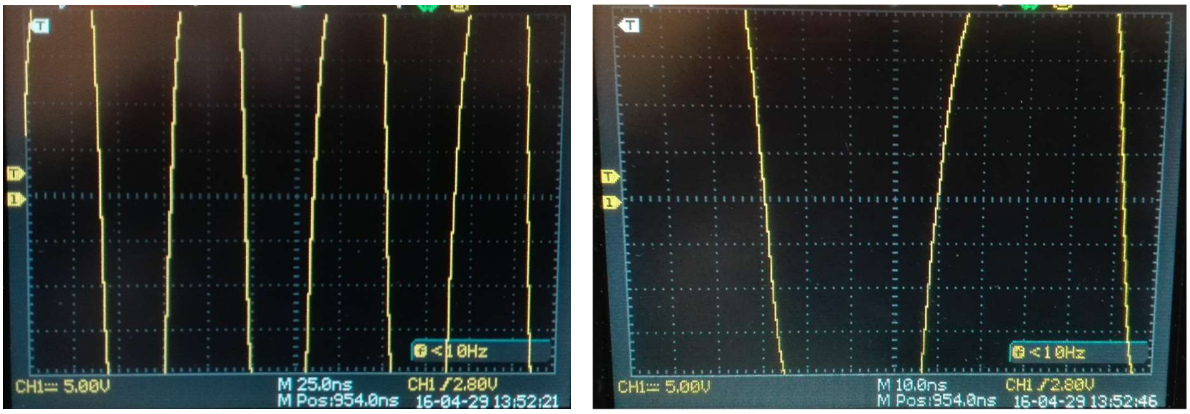

a) **b)**

Figure 19 – RF signal after amplification by the power amplifier as seen on the oscilloscope a) Δt = 25 ns b) Δt = 10 ns.

Figure 19 shows an amplified sine wave from the USRP1, with different time intervals. Both signals are output at full power (1.0x [5]) from the USRP1. This causes the signal to slightly fall outside of the y-axis (V) limit. When the time interval is set at $25\ ns$ (Figure 19a), the signal appears to be a smooth sine wave. However, when the time interval is set at $10\ ns$ (Figure 19b), the signal shows slight distortions near the maxima and minima of the sine wave.

However, the amplified sine wave after the T/R switch is distorted at higher power outputs. This occurs for power output above 0.7x. An example is shown in Figure 20.

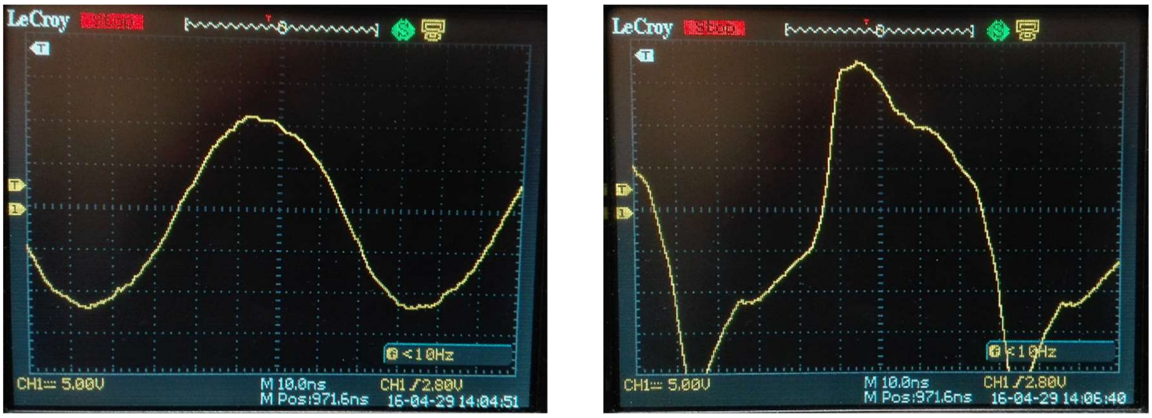

a) **b)**

Figure 20 – Amplified sine wave measured at the probe port of the T/R switch. a) 0.2x power b) 1.0x power.

4.7.3. Preamplifier

The Miteq AU – 1054 was used as the preamplifier. The device had three coaxial ports: one to drive the device ($15\ V$), one input and one output. Saturation of the signal occurs at an input voltage of $\sim 70\ mV$. In the figure below, one can see the amplified RF signal around this saturation value. The signal is amplified up to $\sim 4\ V$ before the maxima and minima get cutoff, as an effect of the saturation. The recovery time is extremely fast, so it can be assumed that any effects from recovery are negligible.

[5] In the rest of this thesis, an output signal from the USRP1 is indicated by the fraction of full power ($0.5\ V$). E.g. at full power and ten percent power, this fraction is 1.0x and 0.1x respectively.

Figure 21 – Saturation of the preamplifier. The preamplifier saturates around 4V with a RF signal at the input of ~70mV.

The results are different when using a passive T/R switch at higher power. Although ring down effects do not seem to appear for short pulses (0.5 μs, Figure 22a), effects do occur for longer pulses. For instance, applying a pulse to the probe for 50 μs at a power of 0.3x causes the preamplifier to have a ring down after the pulse (Figure 22b).

a) **b)**

Figure 22 – Ring down of the preamplifier. A passive T/R switch and probe are connected. The power output is 0.3x. The pulse length is a) 0.5 µs and b) 50 µs.

Thus, ring down effects occur in the preamplifier either because of the high-power output from the power amplifier (after attenuation, $\sim V_{fw}$ remains) or the use of the switch itself.

4.7.4. Passive switch

The research on the switch started with a preliminary model at a resonance frequency of 11.88 MHz. First the results of the use of a physical cable as discussed in the theory section (Chapter 3.2) are outlined. Secondly, the findings of the replacement of this physical cable by a lumped element circuit are shown. Finally, results of several attempts of improvements on this model are outlined.

Physical cable filter tuned at 11.88 MHz

As discussed in chapter 3.2, a switch can be built using a $\lambda/4$ cable. To characterize a switch based on a $\lambda/4$ cable, a series of tests were performed. By taking a coaxial cable with $l > \lambda/4$ and bringing the length down to $l = \lambda/4$ the effect of the length of the cable could be studied. When taking $f_{res} = 11.8\ MHz$, the length of the cable becomes $l = \frac{\lambda}{4} = \frac{16.78}{4} = 4.19m$. In this calculation, the velocity factor is considered: in the medium of a coaxial cable, signals travel at $v = 0.66c$. This follows from the relation:

$$v_f = \frac{1}{\sqrt{\epsilon}} \tag{21}$$

Where v_f is the velocity factor and ϵ the dielectric constant of the material [24]. In the design, only the diodes directly after the transmitter are omitted.

Five lengths were taken and are shown in the table below:

Cable length (m) (±1 cm)	**Signal (V)** (±0.5 V)	**Oscilloscope (V)** (±0.1 V)	**Transmission factor**
6	6	0.84	0.140 ±0.020
5	10	0.76	0.076 ±0.011
4.5	10	0.88	0.088 ±0.011
4.2 *(theoretical value)*	10	0.84	0.084 ±0.011

Table 1 – Data on a series of tests on a switch with a physical coaxial cable.

Although the readout from the oscilloscope was not very accurate (see Table 1), it is evident that a reduction from six meters to five meters is a huge improvement in attenuation. However, once close enough to the target value the difference in attenuation between the different cable lengths becomes less significant.

To measure over a larger set of frequencies, a network analyzer can be used. However, since the network analyzer operates with low voltages and low currents, an adjustment in design is necessary. S12 measurements on the network analyzer are not able to let the protection diodes conduct due to these low voltages, and hence these protection diodes are replaced by a piece of wire to short the circuit. Although this might not fully represent the usage of protection diodes, it should in theory approximately be the same. The results of these measurements are shown in Figure 23.

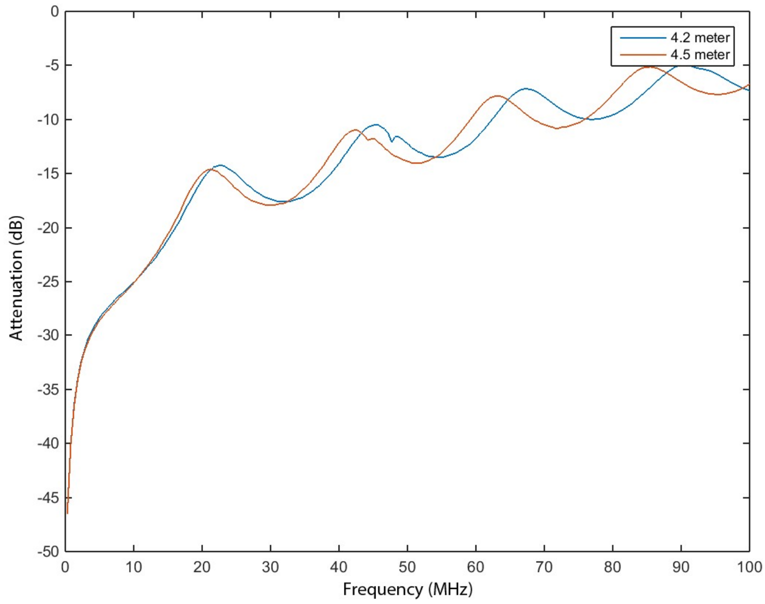

Figure 23 – Two S12 measurements performed on a switch using a cable of $l = 4.5\ m$ and $l = \frac{\lambda}{4} = 4.2\ m$. The attenuation is -23.7 dB and -23.8 dB for $l = 4.5\ m$ and $l = 4.2\ m$ respectively.

As in the measurements performed with the oscilloscope, it becomes clear that a difference in attenuation is insignificant over $\Delta l = 30cm$. However, for higher frequencies the profile is slightly shifted.

Lumped element circuit filter tuned at 11.88 MHz

Calculating the values for the inductor in the π-filter (serving as a replacement for the $\lambda/4$ cable) is done by using equation (12). First a value of C= $270\ pF$ was taken for the capacitor, which resulted in $L = 674\ nH$ for the inductor. These values were not readily available, so two inductors ($422\ nH$ and $246\ nH$) were put in series and two capacitors ($220\ pF$ and $47\ pF$) were put in parallel to create the theoretical values. A S21 measurement on the network analyzer gave an attenuation of -$21.6\ dB$, the same order of magnitude as the $\lambda/4$ cable switch. The dimensions of the switch were rather large ($125\ mm$ by $70\ mm$), thus the switch might be subject to some extra inductance.

In an initial test, the diodes were replaced by rocker switches. From a waveform generator, a sine wave was applied to the Tx-port and read out on the oscilloscope on the Rx-port. The switches closed, gave the following results:

Signal (mV)	**Oscilloscope (mV)** (±0.1 mV)	**Transmission factor**
~9.6 ±0.1	~0.7	0.0745 ±0.011
~32 ±0.5	~1.9	0.0593 ±0.003
~100 ±1	~4.8	0.0480 ±0.001

Table 2 – Data on a series of tests on a switch with a lumped element circuit.

Interestingly, higher voltages lead to greater attenuation. This is possibly due to better conduction at higher voltages, thus creating a better short. The characteristics of the switch over a frequency domain of approximately $50\ MHz$, obtained by the network analyzer, is shown in Figure 24.

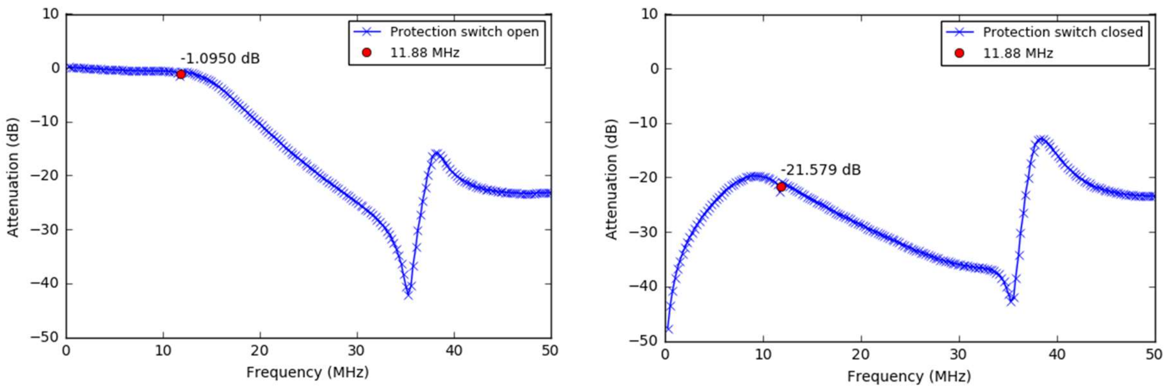

a) **b)**

Figure 24 – a) Characterization of the rocker switch with the protection switch open. Notice the attenuation of approximately -1 dB of any signal picked up by the probe at f_0. b) Characterization of the switch with the protection rocker switch closed. At f_0 the attenuation of the transmission signal is approximately -22 dB.

Conduction of diodes at DC shows forward voltage around $700\ mV$, which is indeed near the forward voltage of the diode. At $11.88\ MHz$ (generated by the waveform generator), the minima and maxima also level to $\pm 700\ mV$. The diodes distorted the minima and maxima of the wave slightly at lower voltages, but this behavior vanishes for voltages higher than $2\ V$.

A first test showed that the power amplifier outputted voltages between $18 - 20\ V$. After attenuation by the filter, $1.36\ V$ of the original signal remained, thus resulting in a signal transmission factor of 0.068. Compared to the "perfect short" (the setup mentioned above with the rocker switches), the attenuation was worse (see last entry of Table 2). A signal of $1.36\ V$ after attenuation would be too high for the preamplifier and since an output voltage of $18 - 20\ V$ is not uncommon in this setup, this caused to be a problem. Two possible reasons for this were: (1) The diodes used in the setup have a small amount of intrinsic capacitance. This might alter the total circuit slightly and cause a less than perfect short for RF signals, thus reducing attenuation. (2) The forward voltage of the diodes is causing a less-than-perfect short. One solution is to increase the number of filters placed in series with one another.

Inductor in series with crossed diodes

To test whether the crossed diodes might have some intrinsic capacitance, a simple test was done by measuring the attenuation after placing an extra inductor in series. The results are listed below in Table 3.

Inductor (nH)	**Power amplifier (V)** (±0.5 V)	**Signal (mV)** (±10 mV)	**Transmission factor**
2.5	14	1080	0.077 ±0.028
5	14	1130	0.081 ±0.029
12.5	14	1160	0.083 ±0.030
33	14	1180	0.084 ±0.030
300 (2x 150 in series)	14	4320	0.309 ±0.110

Table 3 – The results of different sizes of inductors placed directly after the protection diodes. The signal before the filter (power amplifier column) and the signal after the filter (signal column) are shown. The last column shows the transmission factor.

From the last column in Table 3 one can conclude that the transmission factor increases for each addition of inductance. Therefore, intrinsic capacitance of the diodes is not existent or is insignificantly small.

Second filter

The last two possible reasons for a less-than-perfect short (2) and (3) are tested by installing a second filter in series with the first. The second filter was composed of the $\lambda/4$ cable used in the previous experiment (thus being 4.2 m long) and a protection diode. The signals were $11 \pm 1\ V$ and $0.5 \pm 0.1\ V$ from the power amplifier and filter respectively. The transmission factor thus being 0.045. Although this attenuation is larger than the 0.068 mentioned before, the attenuation is much lower than the theoretical values. Since $0.5 \pm 0.1\ V$ is lower than the forward voltage of the diodes, the second set of protection diodes were not working. This was easily tested by placing a wire next to the protection diodes, causing a “perfect short”. The remaining signal was $\sim 40\ mV$, much lower than the forward voltage.

Possibly two filters are needed to reach the correct attenuation. However, a voltage with the order of magnitude of the forward voltage will always remain when using a passive switch. Other diodes with lower voltages, like the Schottky diode, could be used as protection diodes. However, since these diodes generally fall in the range of $0.15 - 0.6\ V$ [25], [26], the preamplifier might still saturate.

Second filter quantification

To quantify the attenuation of two (lumped element) filters in series over a frequency domain of approximately $50\ MHz$, two lumped element filters were put in series and measured with the network analyzer (using rocker switches once again). The results of all possible configurations are shown below in Figure 25.

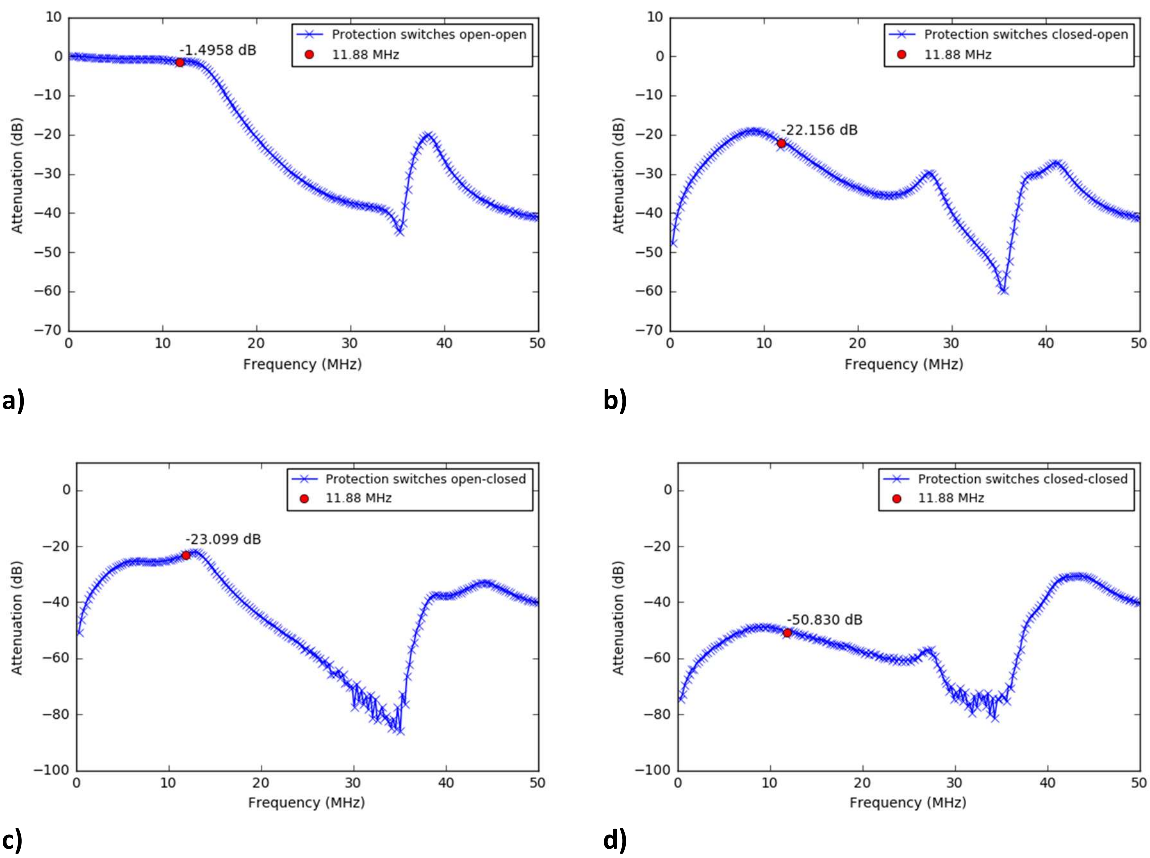

Figure 25 – All possible configurations of two lumped element circuit filters in series, tuned to 11.8 MHz. a) Switch 1 and 2 open. b) Switch 1 closed, switch 2 open. c) Switch 1 open, switch 2 closed. d) Switch 1 and 2 closed.

Comparing Figure 24b with Figure 25d, it can be concluded that addition of an extra filter will attenuate the signal by an extra $-29.51\ dB$ under the assumption of a "perfect short".

4.7.5. Active switch

The highest possible attenuation for N passive filters, is to the level of the forward voltage (V_{fw}) of the crossed protection diodes. To reach higher attenuation, it is possible to use an actively switched filter. An actively switched filter relies on the simple principle of actively shorting at the location of the protection diodes. In other words, the protection diodes are replaced by an electrical circuit allowing for active switching. The implementation of this method is outlined in this section.

PIN diodes and DC output

In the new setup, the protection diodes are replaced by a PIN diode. The theoretical values of the slew rate of PIN diodes are extremely high. Therefore, a PIN diode can be considered as an electrical latch component with TTL logic, when a voltage is applied of either $0\ V$ or a voltage larger than V_{fw}. A DC block of three capacitors in parallel (each $820\ pF$) are placed just before the Tx and Rx port, preventing the DC signal from travelling to the power amplifier or the preamplifier. The matching capacitors on the RF probe serve as a DC block.

The HIGH and LOW of the PIN diode need to be aligned exactly with the ON and OFF state of the pulse respectively. To achieve this, a second output daughterboard in the USRP1 can be used. In this setup, a second LFTX functions at DC outputting $0\ V$ and $0.5\ V$[6] as the HIGH and LOW TTL signal respectively. An initial test, however, was performed using a power supply. The power supply provided a voltage over the PIN diode and a waveform generator applied a continuous RF signal ($11.88\ MHz$) to the filter. The following results were obtained:

Input voltage amplitude RF signal (mV)	**Output voltage maximum RF signal (mV)**	**Transmission factor**
10	0.7 ±0.1	0.070 ±0.010
50	2.2 ±0.1	0.096 ±0.004
100	4.0 ±0.1	0.080 ±0.002
500	22 ±1.0	0.088 ±0.004
1000	35 ±1.0	0.060 ±0.002
2000	110 ±1.0	0.075 ±0.001

Table 4 – Results of an actively switched filter. A continuous (DC) voltage is applied over the PIN diode by a power supply. Column 1: A waveform generator is feeding the system a RF signal at 11.8 MHz. Column 2: The remainder of the RF signal. Column 3: The corresponding transmission factor.

These results are similar to the passive filter results (0.068 attenuation, one filter). However, when a second filter is placed in series a RF generated signal of $2000\ mV$ was reduced to a mere $12\ mV$, resulting in a transmission factor of 0.0085.

These first results could be considered as a proof of concept. Next, correct timing of the DC signal through the LFTX daughterboard had to be incorporated. Changes in the software were easily made

[6] With an input impedance on the oscilloscope of $50\ \Omega$ it is $0.5\ V$. An input impedance of $1\ M\Omega$ gives $1\ V$.

with the GNURadio software (see section 4.9 for more). An extra piece of hardware – an operational amplifier (opamp) – was placed between the LFTX daughterboard and the PIN diode. This had two reasons. One was to protect the sensitive hardware on the daughterboard with the opamp as a separation layer of the two systems. The second reason was to amplify the maximum output voltage of the USRP1, as $0.5\ V$ was below the V_{fw}.

A non-inverting amplifier circuit was used in the setup to amplify the DC signal from the USRP1, the circuit is shown below:

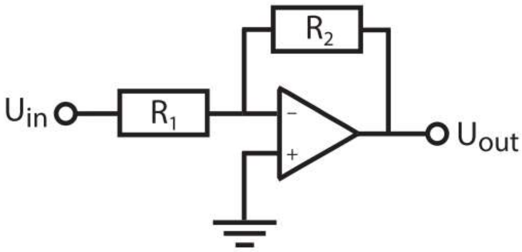

Figure 26 – Non-inverting operational amplifier circuit [12].

Here, the opamp used is the LM358, $R_2 = 220\ \Omega$ and $R_1 = 2.2\ \Omega$. The gain of the signal, G, follows the linear formula [12]:

$$\frac{V_{out}}{V_{in}} = G = 1 + \frac{R_2}{R_1} \qquad (22)$$

With the given values for the resistors, the gain becomes: $G = 101$.

Operational amplifier LM358 tests: switch tuned to 11.88 MHz

Two filters in series, with the opamp connected (in parallel) to the PIN diode did not show similar results to that of the 'proof of concept' tests[7]. The ends of the opamp were connected near the probe port. A continuous DC voltage from a power supply was applied to the opamp. Consequently, the opamp delivered a higher voltage to the PIN diode. The voltage over the PIN diode was measured while a continuous RF signal was applied to the system. This RF signal was raised from $700\ mV$ with increments of $100\ mV$ up to $1000\ mV$. The voltage over the PIN diode remained $637\ mV$ up to $900\ mV$. However, at $1000\ mV$ the system broke down and a small negative voltage ($-20\ mV$ to $-50\ mV$) over the PIN diode remained. A potential explanation for this behavior is interference of the RF signal with the opamp, causing the opamp to break down. A potential solution thus might be to incorporate RF chokes between the ends of the opamp and the ends of the PIN diode.

Some further tests are shown in Figure 27. As in the first test, breakdown occurs when the opamp is connected near the probe port (Figure 27a). Although adding a RF choke does seem to shift breakdown to a higher voltage, it does not appear entirely. Only when the opamp is connected directly next to the (first) PIN diode (Figure 27b), this behavior disappears.

[7] In this test, the second filter was newly built, with approximately half the size of the original filter circuit board. This second filter was tuned to $11.88\ MHz$, attenuated the signal (at f_{res}) by $-28.7\ dB$ when shorted (thus $\sim -3\ dB$ better than larger version) and attenuated the signal (at f_{res}) by $-0.50\ dB$ when open.

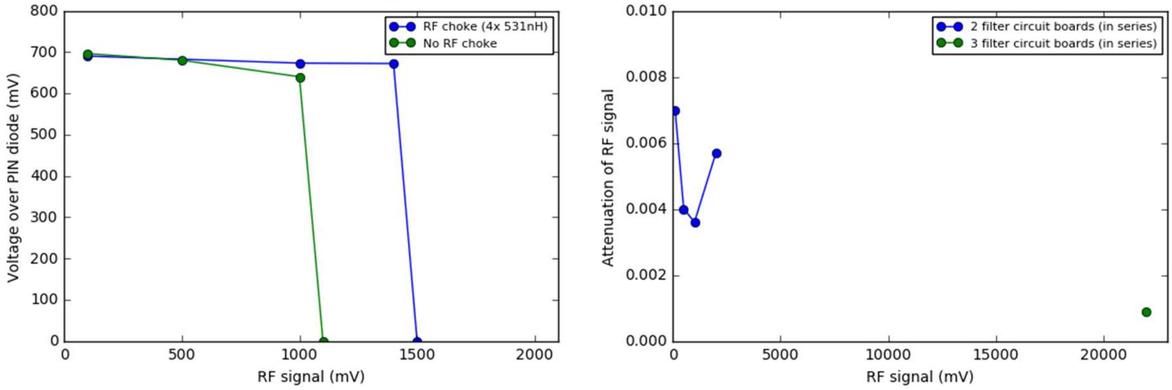

a) **b)**

Figure 27 – a) The opamp is connected near the location of the probe port, 2 filter circuit boards are placed in series. The PIN diode stops working when the RF signal is 1100 mV and 1500 mV. After adding a RF choke, breakdown occurs at a higher voltage. b) The opamp is connected directly next to the first PIN diode. The opamp maintains operation, even with 3 boards at 22 V. The data shows higher attenuation when an extra circuit board is added, as is to be expected.

Timed operational amplifier LM358 tests: switch tuned to 11.88 MHz

The results (Figure 27b), show good attenuation with use of an opamp. This section elaborates further on the use of the operational amplifier and the inclusion of timing. A new RF probe was built and used in these experiments, tuned at 12.4 MHz.

A first simple test with a Tx/Rx sequence was done with the RF signal between 0.3x to 0.7x and a pulse width of 50 μs[8]. Next to attenuation of the pulse, another signal can be seen shortly after the pulse with a decaying shape. This behavior is shown in Figure 28 and is not present in a spin-echo sequence.

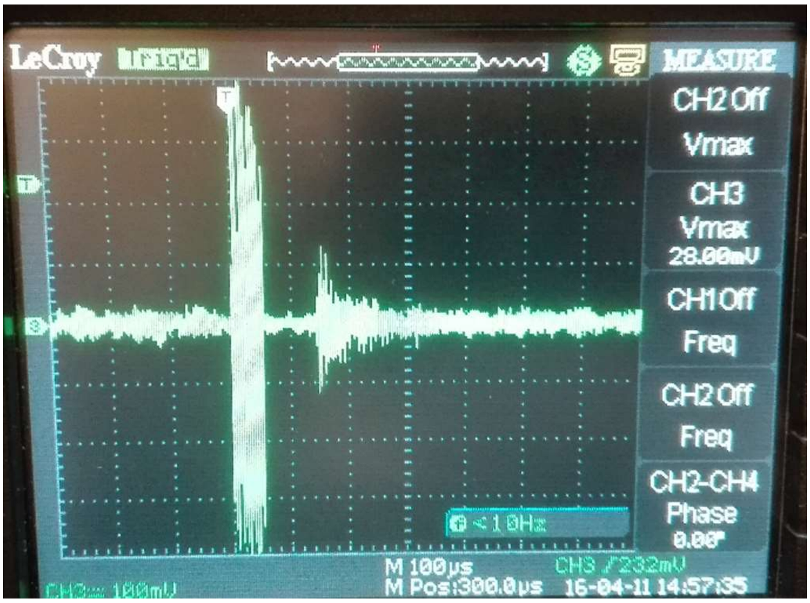

Figure 28 – The first signal is the attenuated RF pulse. The second signal is unexpected behavior, with a decaying shape. This signal appears ~100 µs after the RF pulse.

The second signal is unexpected. The maximum of this signal is the lowest without the RF probe attached, increases when the coil is attached and inside the magnet and is the largest when the RF probe is inside the magnet with a phantom in the coil. The signal fades for RF pulse power settings

[8] In these first tests the filter board tuned at 11.88 MHz was used. However, since 12.4 MHz differs only slightly (0.5 MHz), the behavior is approximately the same.

>0.7x. For a complete overview of this behavior, refer to the images at different RF pulse power settings in Appendix 2. Here the timing of the RF pulse and according DC block pulse are not the problem. This is performed perfectly by the USRP1 hardware and software (for more, see Section 4.9).

Further tests on the hardware side of the DC pulse were performed. The PIN diode response to a DC pulse from the USRP1 was analyzed. In Figure 29 the results are shown.

a) **b)** **c)**

Figure 29 – Response function from the PIN diode (blue) to a square wave (green). The wave is amplified by the operational amplifier, the wave shown is before amplification. The square wave varies between 0 V and a) 10 mV, b) 20 mV and c) 40 mV. The slew rate at the end of the response remains the same throughout a-c). The slew rate at the front increases with the voltage output from the square wave. Note the little peak in c) at the beginning of the response at higher voltages.

It becomes clear that the PIN diode response to a square wave is not a square wave at all. The slew rate at the front is low for low voltages, but increases with each increment in voltage. The slew rate at the end of the PIN diode response remains low for each voltage level. Notice the time frame of the pulse: 250 μs. For pulses around 50 μs the PIN diode needs half this time to reach the correct voltage and almost twice this time to revert back to $0\ V$. This is illustrated in Figure 30.

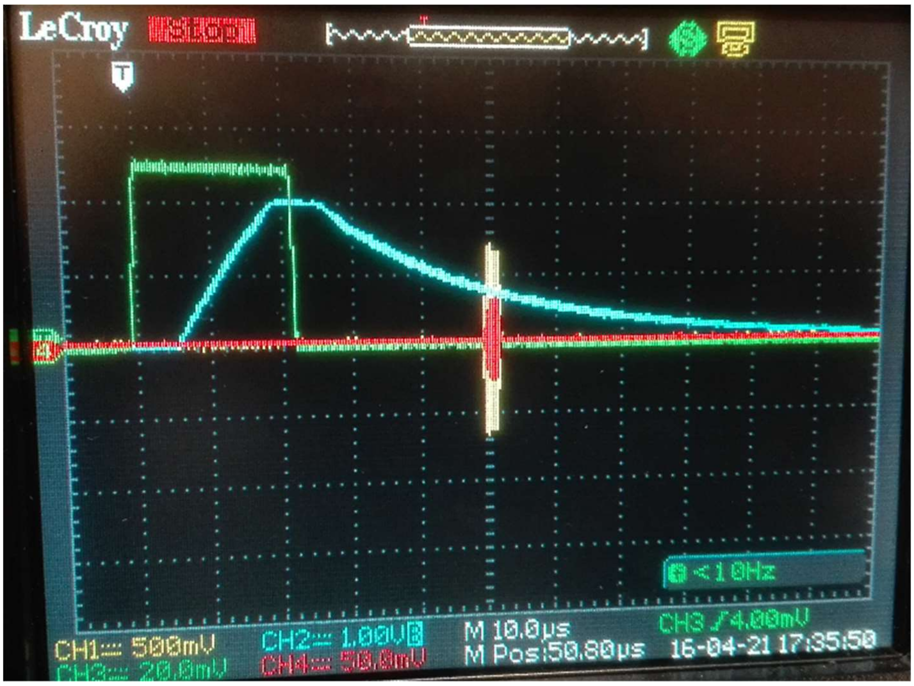

Figure 30 – Green: *operational amplifier DC pulse (gain 0.1x, width 20 µs).* Blue: *PIN diode response function to the DC pulse.* Red: *RF pulse from the USRP1.* Yellow: *RF pulse after the power amplifier.*

Moreover, in this figure a potential solution is shown. By perfectly timing the RF pulse (red and yellow), the RF pulse during transmission will be blocked but, due to voltages deemed too low for conduction of the PIN diode, a signal NMR signal might be received. This setup, however, was not further investigated as this was not considered a perfect solution. Furthermore, the exact timing would be extremely hard to achieve, as it differs for every pulse width and pulse voltage. The use of a faster opamp and a square wave between positive and *negative* voltages, would potentially increase the PIN diode response function.

Lumped element circuit filter tuned to 12.4 MHz

This section describes the development of a new series of filters tuned to 12.4 MHz. This is the frequency in the exact center of the magnet. First the value used for the inductor was set at $L = 641\ nH$, composed of a $531\ nH$ and $110\ nH$ inductor in series. Equation (12) then dictates that the theoretical value for the capacitors is $C = 257\ pF$. Here three capacitors were taken in parallel: $240\ pF$, $10\ pF$ and a variable capacitor between $5 - 90\ pF$. The results of the three newly build filters are shown in Figure 31 and could be placed in series for higher attenuation. The DC blocks used have the same values as before.

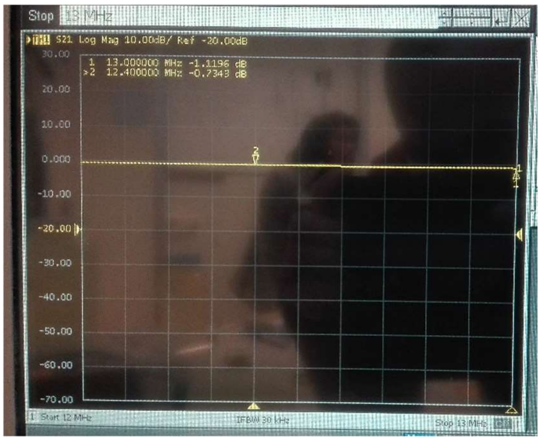

a)

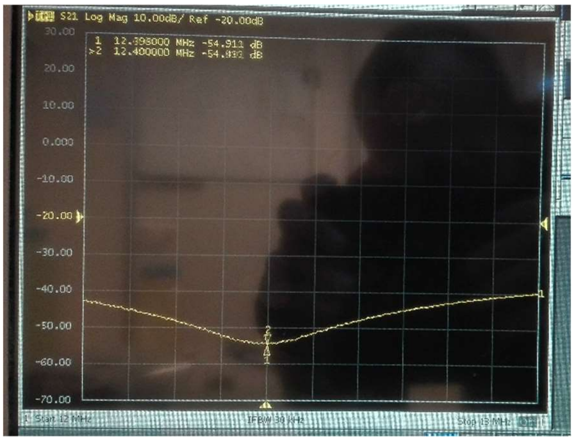

b)

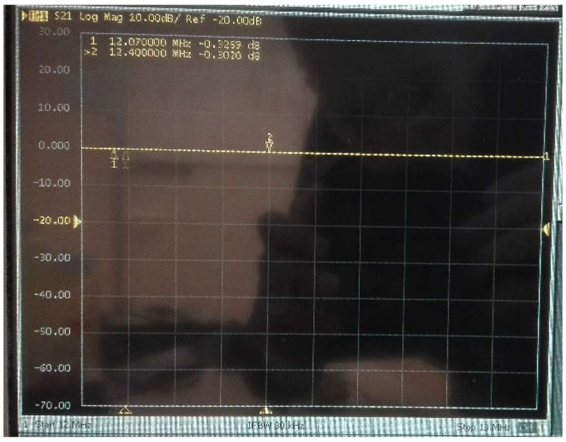

c)

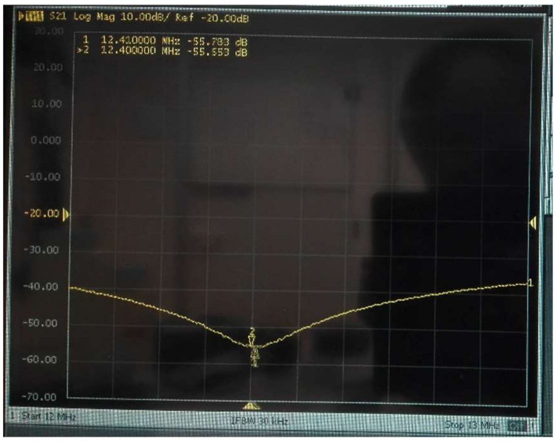

d)

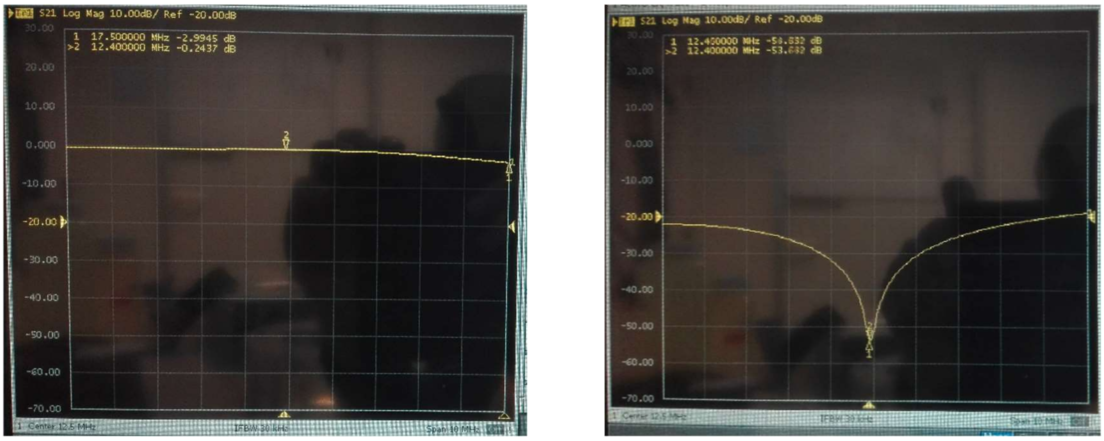

e) **f)**

Figure 31 – Results of 3 filter boards tuned at 12.4 MHz. All ON/OFF states are simulated by using a rocker switch at the protective diode location. a, b) Filter 1, switch open and closed respectively. c, d) Filter 2, switch open and closed respectively. e, f) Filter 3, switch open and closed respectively.

One can easily observe that the newly build filters are far more efficient than the filters tuned to $11.88\ MHz$. The discovery of a ground loop has led to this increase of efficiency. The removal of the right connection to ground on the coaxial Tx port, removed the ground loop.

An impulse response test to a square wave was also performed on the first filter, to see the effect of the DC blocks to the DC pulse. The capacitors seem to charge and discharge with the square wave accordingly. The effect is shown in Figure 32. In the literature, this effect is referred to as video leakage [27].

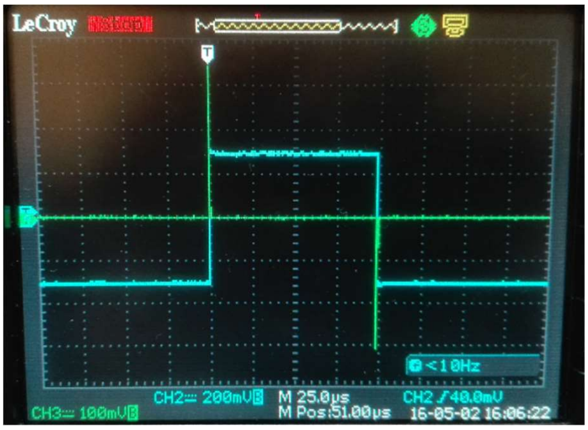

Figure 32 – Impulse response function of filter 1 to a square wave.

Final switch configuration

After all the tests performed and outlined in this section, the final switch setup was as follows:

- To get the correct attenuation, first a passive switch is used to bring the voltage down to the level of the protection diode ($\sim 600\ mV$). This passive switch was bought, but as previously shown, can also be constructed by using a $\lambda/4$ cable or a π-filter section;
- In series is an active switch build to the same design as before, to attenuate the RF pulse even more. The only alteration in design is near the protection diode (see Figure 33) and the protection diode itself (BA182);
- The driving of the PIN diode is done with the operational amplifier opa627. A new driver design is used to drive the PIN diode with between voltages of $-3\ V$ and $0.6\ V$ (see Figure 34).

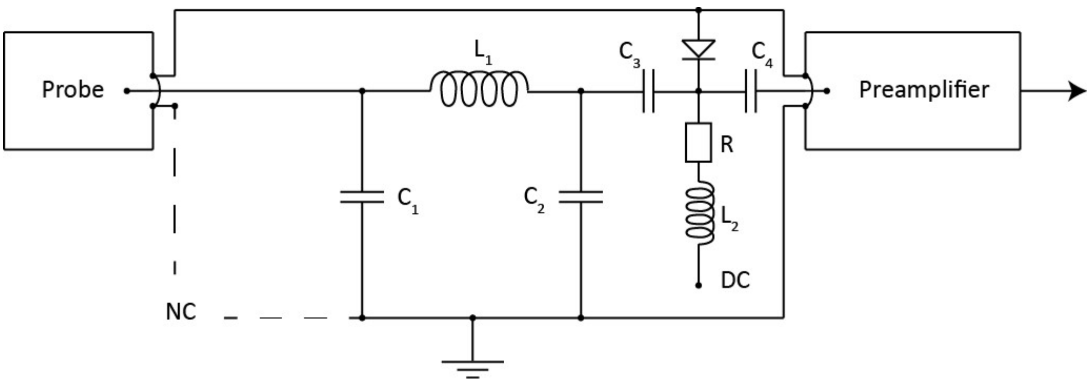

Figure 33 – The final T/R switch configurations. The π-filter design. $R = 100\ \Omega$, $L_2 = 47\ \mu H$ and $C_3 = C_4 = 10\ nF$.

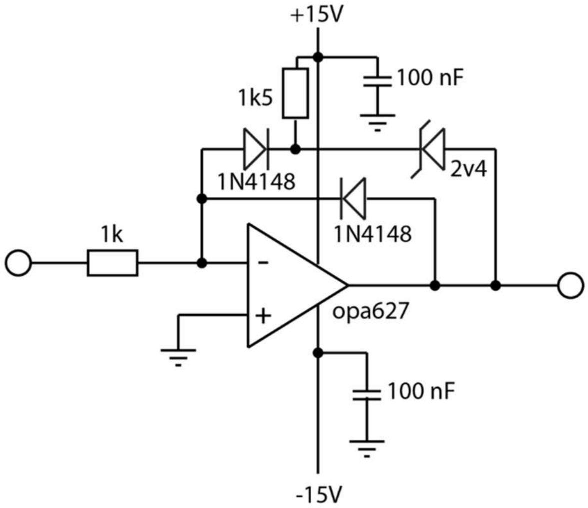

Figure 34 – The PIN diode driver.

The first test done with the new configuration as in Figure 33 showed promising results. In this test, the passive filter consisted of a classic $\lambda/4$ cable design with crossed diodes. Moreover, the π-filter section was also replaced by a $\lambda/4$ cable. A RF signal ($12.4\ MHz$) was continuously applied to the two filters and measured directly after the second (active) filter. The result is shown in Figure 35.

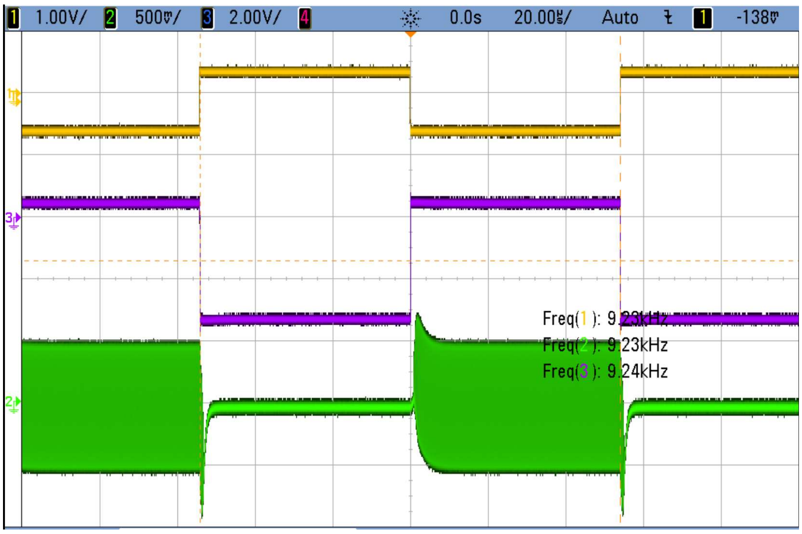

Figure 35 – A RF signal is continuously applied to the two filters in series (passive – active). This signal is directly measured after the second filter (green). The TTL signal is either +0.5 V or -0.5 V (yellow). The signal after amplification by the opa627 is +0.6 V and -3 V respectively (purple).

Clearly the ON/OFF state of both the TTL signal and the amplified TTL signal is reflected in the attenuation of the RF signal. The exact setup as in Figure 33, provided similar results. With a RF pulse of 0.3x power (at 12.4 MHz), the pulse was attenuated down to approximately 20 mV; low enough to apply to the preamplifier without saturation. This result is shown in Figure 36.

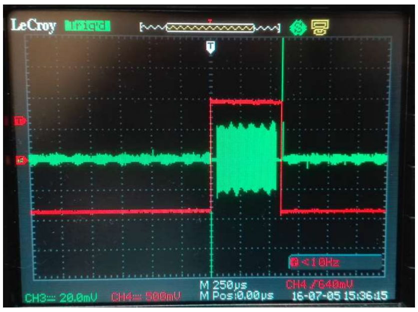

Figure 36 – Attenuation of a RF pulse at 0.3x power and 12.4 MHz (green). The TTL signal is directly measured from the USRP1 (red)[9].

Another test was performed to measure the attenuation and noise in a NMR signal after the passive and active filter. The results of this test are shown Figure 37, where one can see the attenuation and noise in a 5 mV signal.

a) **b)** **c)**

Figure 37 – Measurements of attenuation and noise of a 5mV NMR signal after a) the passive switch, b) the passive switch and the π-section and c) the passive switch, the π-section and the DC driver connected.

[9] Input impedance on the oscilloscope was 1 $M\Omega$ for this measurement

It is evident that noise added to the signal originates primarily from the π-section and the DC driver. Signal attenuation in the figures is non-existent after both the passive and active filter. This is rather unexpected, since attenuation of a signal at $12.4\ MHz$ was between 0 and $-1.5\ dB$ for any active filter with a π-section design. Moreover, a network analyzer measurement of the attenuation of the specific π-section filter used in the final configuration confirms this as well: At f_0 an attenuation exists of $-0.32\ dB$ (Figure 38a) with the latch opened. The attenuation with the latch closed was $-29.7\ dB$ (Figure 38b). This attenuation is not as high as previously designed π-section filters and thus a suggestion for future research is to try to increase the attenuation even further.

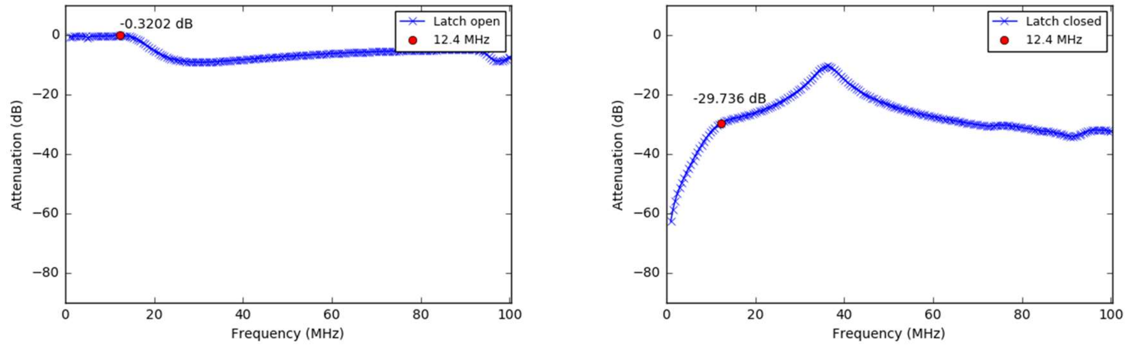

a) **b)**

Figure 38 – Attenuation of a signal in the frequency domain of 1 MHz – 100.3 MHz after the π-section filter with a) the latch opened and b) the latch closed.

4.8. Total setup overview

In the previous sections the individual hardware components are discussed. The final setup with all interconnected individual hardware components as used in this research is shown in the image below.

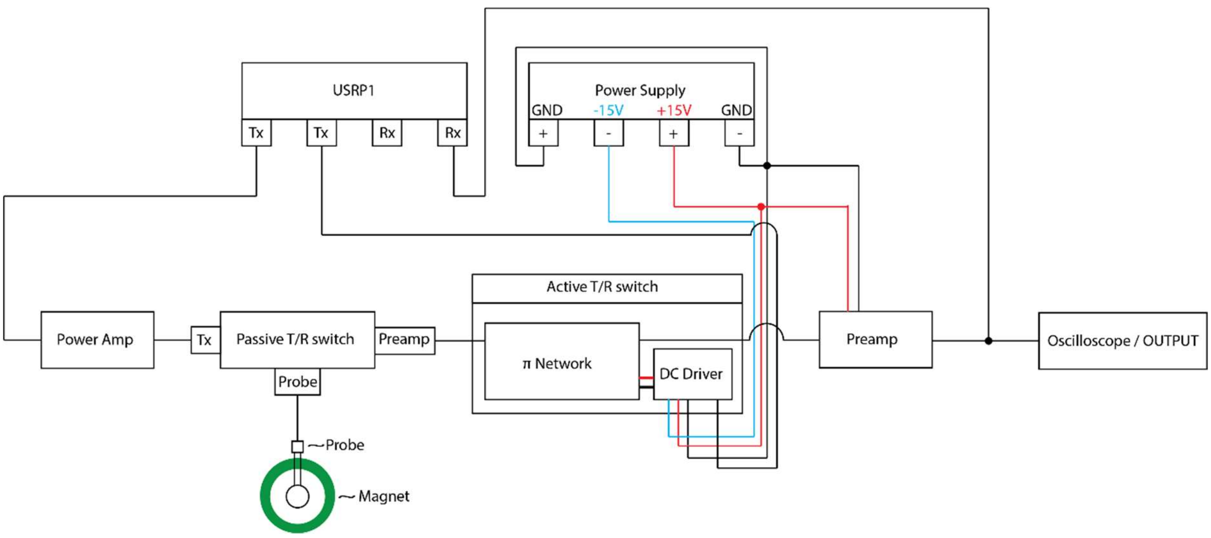

Figure 39 – Overview of the final setup. Notice the transmission lines of the RF pulse and the DC (protection) signal from the USRP1 Tx ports. After the preamplifier, a signal is picked up by the USRP1 Rx port and/or the oscilloscope.

A RF signal is transmitted from one of the two Tx ports on the USRP1, traveling through the power amplifier, the passive T/R switch and finally the RF probe. A generated NMR signal travels back through the passive and active T/R switch, preamplifier and finally the USRP1 Rx port and/or the oscilloscope. During transmission and reception, the active switch is turned on and off accordingly by a DC signal travelling from the (second) USRP1 Tx port to the DC driver. The DC driver itself is powered by a power supply with $+15\ V$, $-15\ V$ and GND. The preamplifier is powered from the same power supply with $+15\ V$ and GND.

4.9. Software

The recommended OS for the GNURadio software is Linux and was thus used on a PC with the USRP1 connected to one of the USB-hubs. In this research, only the visual editor of the GNURadio Companion was used to create a basic, dynamical transmit-receive application. The basis of the application was initially build on the code provided by the thesis of C.J. Hasselwander [6], but was quickly altered for custom features. The application can output on two channels (the RF pulse and blanking signal for the DC driver) and receive on a third channel. This section will go through the main components in detail. The main components are highlighted in Appendix 3.

RF pulse

A square wave is created by the Signal Source block and adjusted to output a RF pulse from the USRP1 (Appendix 3, red sections). To get the correct pulse width, two signals are multiplied. One is the original signal, the second is altered in the following way:

1. A constant of -1 is added to the signal. The maximum (+1) becomes zero, zero becomes the minimum (-1);
2. The square wave is then multiplied by a constant of -1, which results in the original signal only 180° out of phase;
3. Finally, the second signal is delayed and dependent on a variable called tx_samps.

The pulse width depends on the variable tx_samps and the sample rate ($samp\_rate$) in the following way:

$$PW = \frac{tx\_samps}{samp\_rate} \tag{23}$$

With a slight overlap of tx_samps, multiplication of the original signal and the altered second signal result in a pulse of length PW. This process is illustrated in Figure 40. The blue rectangles indicate the overlapping area between the original signal and the altered signal, corresponding to the pulse. The pulse is delayed by $pulse\_delay$, a variable indicating the delay of the pulse after the start of the blanking signal (see also next subsection). The pulse signal is converted to a complex number and multiplied by a constant. This constant is the amplitude of the signal (default value is zero) and can be dynamically adjusted when running the application. Lastly, the signal terminates in an USRP Sink, which determines the frequency of the RF pulse (i.e. the signal is multiplied by a sine wave and outputted by the hardware). The frequency is determined by the variable $center\_freq$.

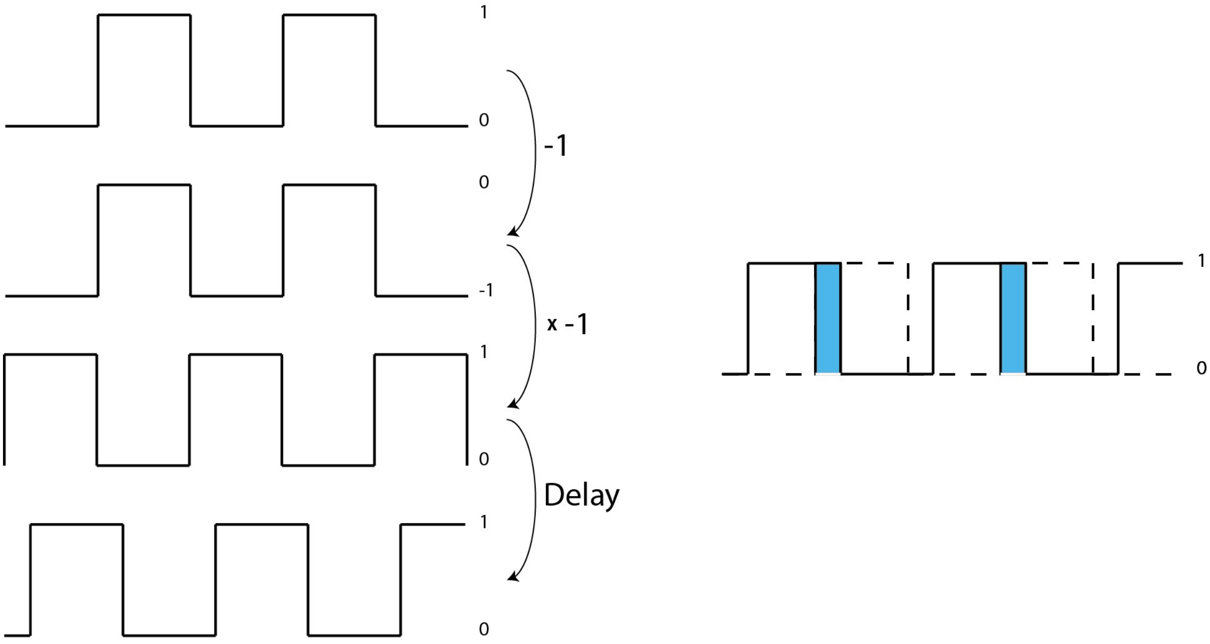

Figure 40 – Creation of the RF pulse. Left: mathematical operations applied to the original signal (top square wave), resulting in an altered signal (bottom square wave). Right: multiplication of the original signal with the altered signal, resulting in the required RF pulse width.

Blanking signal

The blanking signal for the DC driver is generated in a similar way as the RF pulse (Appendix 3, blue sections). There are two differences:

1. The delay is defined as $PW + pulse\_delay + pulse\_delay\_end$;
2. After multiplication, the signal is split up for a second time. A constant of -1 is added to one of the two signals, creating a square wave 180° out of phase and the maxima transposed to minima.

As mentioned in the previous subsection, $pulse\_delay$ is the amount of time for the RF pulse to start after the blanking signal is turned on. The variable $pulse\_delay\_end$ is the amount of time for the blanking signal to terminate, after the termination of the RF pulse. To satisfy the experimenters' needs, the blanking signal can be tweaked (in relation to the RF pulse) while running the application. The adjusted signal then terminates in the USRP Sink at a frequency of zero (DC output). The blanking signal in relation to the RF pulse are schematically illustrated in Figure 41.

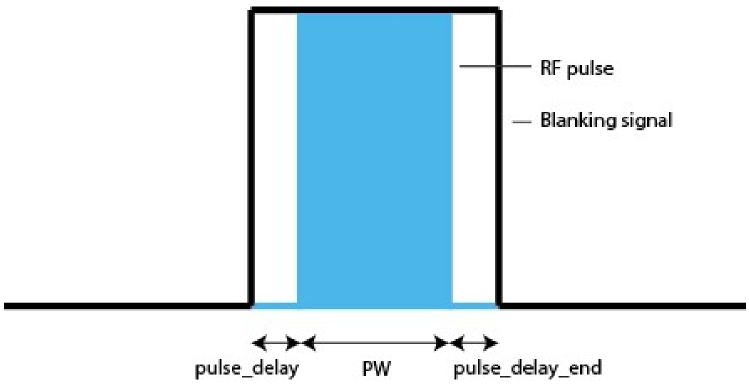

Figure 41 – The blanking signal (black) and the RF pulse. PW is the pulse width. The length of $pulse\_delay$, $pulse\_delay\_end$ and the amplitude of both the RF pulse and the blanking signal can be dynamically adjusted during transmission.

Square wave generator

The square wave is generated by the Signal Source block (Appendix 3, purple section). The period of the square wave used for the RF pulse and the blanking signal, should at least be PW long. At this very minimum, the RF pulses are of the same length as the dead time. This is obviously inconvenient and a TR time variable is taken into the equation. Thus, the frequency for the square wave becomes:

$$f = \frac{1}{TR + PW} \tag{24}$$

Scope

The input of the USRP1 (USRP Source block) is attached to a WX GUI Scope Sink (Appendix 3, green section). The Scope Sink functions like an ordinary oscilloscope, with one small differences. The Scope Sink uses an adjustable reference frequency. In this research, the frequency ($cent\_freq$) is set before running the application.

5. Conclusion and Outlook

5.1. Conclusion

This research aimed to design and characterize a hardware and software acquisition system for low field MRI. The system's architecture consisted of three major components: the software, the transmit-receive system and the hardware. The software used was GNURadio and an application was written in the GNURadio Companion visual editor, using previous research as the basis of the program [6].

The application performed a simple transmit-receive sequence, but the GNURadio application can easily be altered, providing high customizability for other sequences. The GNURadio application can be loaded to the USRP1.

This Software Defined Radio replaced complex custom built transmit-receive systems (usually involving Field Programmable Gate Arrays). Moreover, the relatively low cost of the SDR (approximately 1000 US dollars) provides a great cost reduction in contrast to conventional MRI scanners.

The hardware consisted of a power amplifier, a Transmit-Receive switch, a RF probe, a preamplifier, and permanent magnets in a Halbach array. Again, all these components have a relatively low price and are small enough to move.

In conclusion, the total system had a low cost, was portable and customizable. However, the performance of the MRI scanner is a question that remains open. A NMR signal in the form of a Free Induction Decay remains yet to be detected. This might be due to several reasons. The most plausible underlying causes, in conjunction or not, are:

1. The inability to see a signal during real-time reception. Although the signal of the RF pulse is attenuated, the fraction seen on either the oscilloscope or the scope on the PC remains multiple orders larger than the NMR signal. This makes it hard to determine a potential FID;
2. Malfunctioning hardware. Especially the T/R switch proved to be a not so trivial hardware component. The characterization of this piece of equipment has been described in the result section in detail, but several questions remain open. Measured attenuation of a potential NMR signal on an oscilloscope did not fully correspond to the measured attenuation on the network analyzer. The primary noise source was the active switch;
3. The inhomogeneities and strength of the B_0 field. This might be why there is no FID seen at all. Relaxation related to inhomogeneities is characterized by the T_2^+ time and ultimately by the T_2^* time as described by equation (10). The signal strength scales with B_0^2 and the noise with $B_0\sqrt{B_0}$ (for more details, see Chapter 3).

5.2. Suggestions for future research

For follow up research the most plausible causes can be investigated:

1. To record data from signals on the USRP1 input, one could use a package like gr-MRI [6] or write new blocks in Python or C++ that save the data to files (e.g. CSV files). This makes analyzing the acquired signals much easier;
2. The T/R switch could be closer inspected and improved by further research. For instance, investigating what the true attenuation of a NMR signal is and where the noise in the active switch is originating from are questions that might be worth answering. Especially the latter, since the noise can potentially be reduced;

3. To be able to investigate both the first and the second point, complete elimination of inhomogeneities in the B_0 field are very useful. For prototyping, it thus might be very useful to use a (expensive) low field NMR scanner with a proven homogeneous B_0 field. Especially if such a scanner comes with hardware; first the recording software and SDR can be tested before testing the hardware system researched.

The function of the full system depends on all three previously mentioned points. To determine if the full system is functioning properly (i.e. detection of a FID), each point should be investigated individually before testing the complete setup.

References

[1] R. Damadian, M. Goldsmith, and L. Minkoff, "NMR in cancer: XVI. FONAR image of the live human body," *Physiol. Chem. Phys.*, vol. 9, no. 1, pp. 97–100, 1977.

[2] L. Glover, "Why Does an MRI Cost So Darn Much? | MONEY," *Money Magazine*, 2014. [Online]. Available: http://time.com/money/2995166/why-does-mri-cost-so-much/. [Accessed: 12-Jun-2017].

[3] N. Smith and A. Webb, *Introduction to Medical Imaging*. Cambridge University Press, 2011.

[4] Michael L Johns, *Mobile NMR and MRI: Developments and Applications*. Royal Society of Chemistry, 2015.

[5] K&J Magnetics, "AY0X030-S." [Online]. Available: https://www.kjmagnetics.com/proddetail.asp?prod=AY0X030-S&cat=168. [Accessed: 02-Aug-2016].

[6] C. J. Hasselwander, "gr-MRI: A Software Package for Magnetic Resonance Imaging Using Software Defined Radios," Vanderbilt University, 2016.

[7] M. S. Wijchers, "Image Reconstruction in MRI," TU Delft, 2016.

[8] Wikipedia and GyroMagician, "File:Nmr fid good shim EN.svg," 2013. [Online]. Available: https://commons.wikimedia.org/wiki/File:Nmr_fid_good_shim_EN.svg. [Accessed: 21-Mar-2017].

[9] J. Mispelter, M. Lupu, and A. Briguet, *NMR probeheads for biophysical and biomedical experiments : theoretical principles & practical guidelines*. Imperial College Press, 2006.

[10] C. Chen and D. I. Hoult, *Biomedical Magnetic Resonance Technology*. Taylor & Francis, 1989.

[11] F. R. Connor, *Wave Transmission*. Edward Arnold, 1972.

[12] J. J. T. Wagenaar, *Signal detection and Signal detection*, 3rd ed. Leiden: Leiden University, 2014.

[13] S. Sykora, "Suppression of receiver recovery time in NMR," *Stan's Libr.*, vol. 2, 2007.

[14] D. J. Griffiths, *Introduction to electrodynamics*, 4th ed. Prentice Hall, 2012.

[15] W. Tang, H. Sun, and W. Wang, "A digital receiver module with direct data acquisition for magnetic resonance imaging systems," *Rev. Sci. Instrum.*, vol. 83, no. 10, pp. 0–7, 2012.

[16] A. Asfour, K. Raoof, and J. P. Yonnet, "Software Defined Radio (SDR) and Direct Digital Synthesizer (DDS) for NMR/MRI instruments at low-field," *Sensors (Basel).*, vol. 13, no. 12, pp. 16245–16262, 2013.

[17] GNURadio, "GNURadio Software," 2017. [Online]. Available: https://www.gnuradio.org/about/. [Accessed: 16-Feb-2016].

[18] GNURadio, "GNURadio Guided Tutorials," 2017. [Online]. Available: https://wiki.gnuradio.org/index.php/Guided_Tutorials. [Accessed: 16-Feb-2016].

[19] K&J Magnetics, "AY0X030-C." [Online]. Available: https://www.kjmagnetics.com/proddetail.asp?prod=AY0X030-C&cat=168. [Accessed: 02-Aug-2016].

[20] K&J Magnetics, "AY0X030-N." [Online]. Available: https://www.kjmagnetics.com/proddetail.asp?prod=AY0X030-N&cat=168. [Accessed: 02-

Aug-2016].

[21] K&J Magnetics, "Glossary of Magnet Terminology." [Online]. Available: https://www.kjmagnetics.com/glossary.asp#Plating. [Accessed: 02-Aug-2016].

[22] S. H. I. Lio, "Magnetic Field Measurement," 2014. [Online]. Available: http://www.stanleylio.com/home/magnetic-field-measurement. [Accessed: 01-Apr-2016].

[23] P. Jansen, "Measuring Magnetic Fields in a Volume," 2015. [Online]. Available: https://hackaday.io/project/5030-low-field-mri/log/16020-measuring-magnetic-fields-in-a-volume#header. [Accessed: 01-Apr-2016].

[24] I. Poole, "Coax Cable Velocity Factor." [Online]. Available: http://www.radio-electronics.com/info/antennas/coax/coax_velocity_factor.php. [Accessed: 20-Mar-2017].

[25] Future Electronics, "What is a Schottky diode?" [Online]. Available: http://www.futureelectronics.com/en/diodes/schottky-diodes.aspx. [Accessed: 20-Mar-2017].

[26] Vishay Semiconductorers, "1N5817-1N5819 Schottky Barrier Rectifiers Datasheet." 2002.

[27] D. O. Brunner, L. Furrer, M. Weiger, W. Baumberger, T. Schmid, J. Reber, B. E. Dietrich, B. J. Wilm, R. Froidevaux, and K. P. Pruessmann, "Symmetrically biased T/R switches for NMR and MRI with microsecond dead time," *J. Magn. Reson.*, 2016.

Appendix

1. Materials

Object	**Company**	**Model**
Network analyzer (old)	Agilent Technologies	E5061A
Network analyzer (new)	Copper Mountain Technologies	PLANAR TR1300/1
RF wave generator	Agilent Technologies	N9310A
RF wave generator	Agilent Technologies	33500B
PC	HP	Linux OS
Software Defined Radio (SDR)	Ettus Research	USRP1
SDR daughter boards	Ettus Research	LFTX & LFRX
RF power amplifier	Electronic Navigation Industries	310 L
(Passive) T/R switch	NMR Service GmbH	
DC power supply	Tenma	72-10500
Preamplifier	MITEQ	AU - 1054
Oscilloscope	LeCroy	WaveAce 234
Permanent magnets	K&J Magnetics	AY0X030-S, AY0X030-N, AY0X030-C
Gaussmeter (old)	Unkown	Unkown
Gaussmeter (new)	AlphaLab Inc.	GM-2
Lasercutter	VersaLASER	Laser 2000

2. Ring down after RF pulse

This appendix shows ring down after a pulse for several power levels. The RF pulse lasts 50 µs, the ringdown occurs approximately 100 µs after the pulse. The power output from the USRP1 is indicated below each image. Counts show the fraction of the maximum voltage the USRP1 can handle (i.e. 0.5 V).

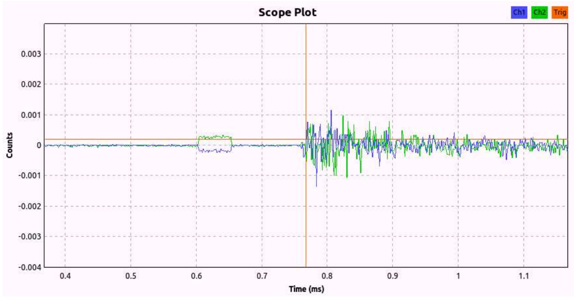

0.025x

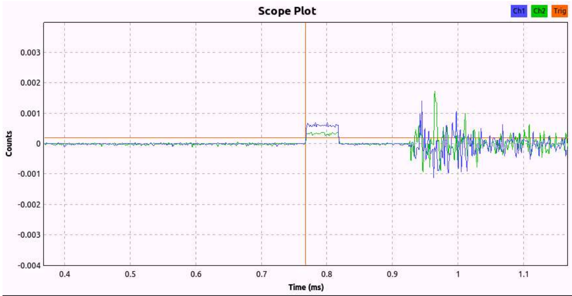

0.05x

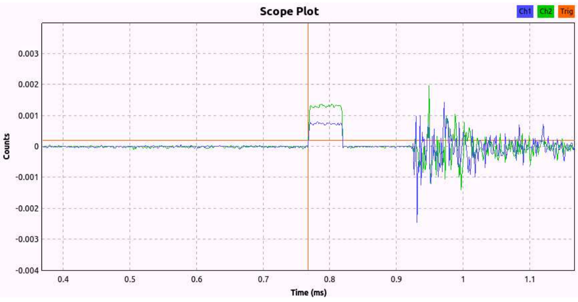

0.1x

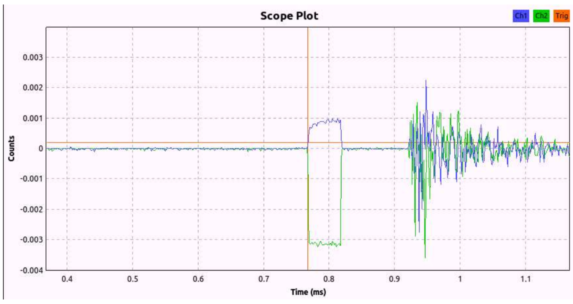

0.2x

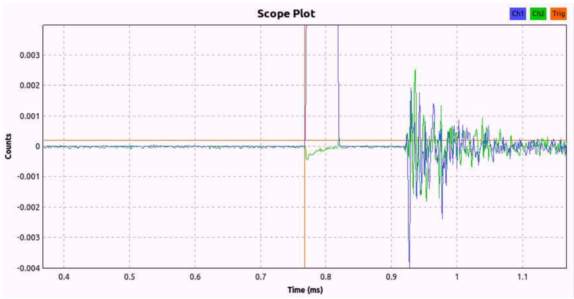

0.3x

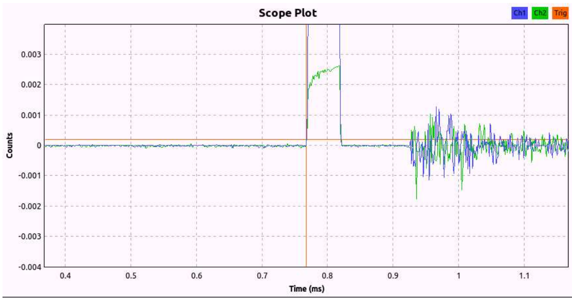

0.4x

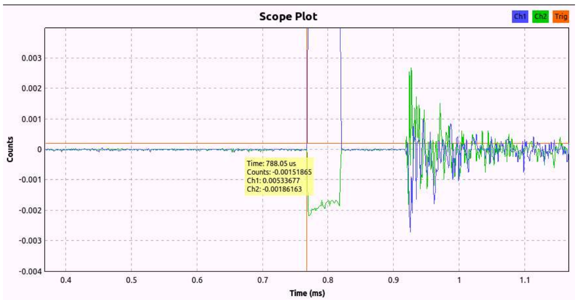

0.5x

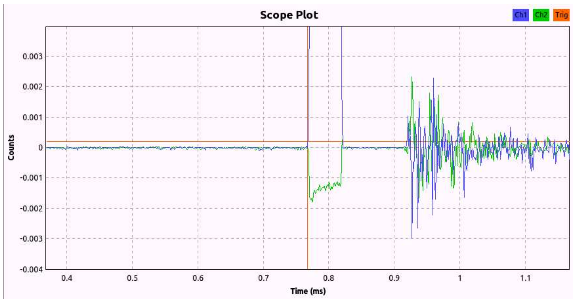

0.6x

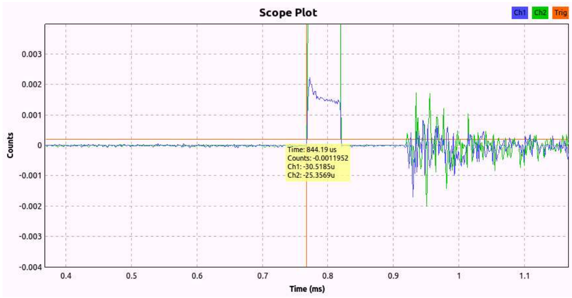

0.7x

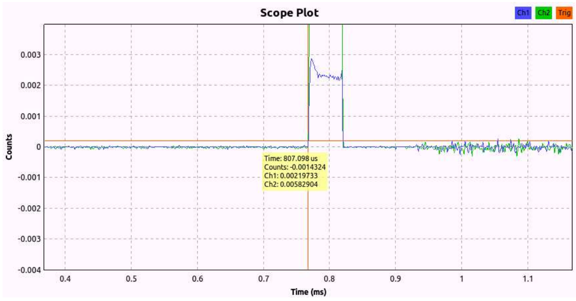

0.8x

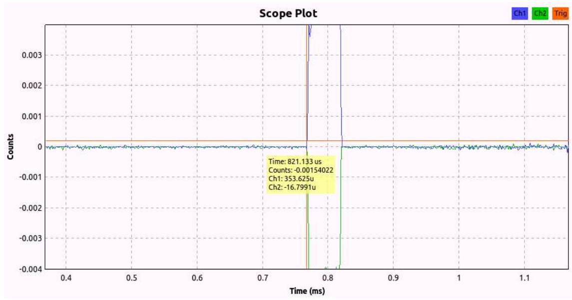

0.9x

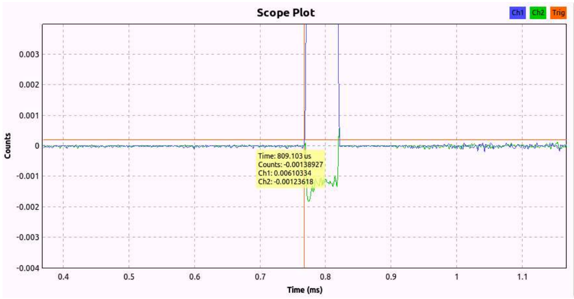

1.0x

3. Transmit-receive GNURadio Application

Overview of the GNURadio transmit-receive application. The Options and WX GUI Notebook blocks take parameters determining the visual appearance of the application. Variable blocks are constants and must be setup before running the application. Slider and Chooser blocks are dynamically adjustable variables. The main components are highlighted. These are:

- The RF pulse (*red*);
- The blanking signal (*blue*);
- The signal source, creating a square wave (*purple*);
- The USRP input and scope (*green*).